Acoustic Propagation in non Reacting Flows

MC Polka Network week 3
Scientific Lecture # 3

Hadrien Bériot[1], Sophie Le Bras[1], Gwénaël Gabard[2]

[1] Siemens Industry Software N.V., 3001 Leuven, Belgium
[2] LAUM, Le Mans University, 72000 Le Mans Cedex 9, France

hadrien.beriot@siemens.com

24th November 2020

Introduction

1. Provide an overview of acoustics convected propagation models:
   - Physical models.
   - Computational schemes.
   - Structured vs unstructured.
   - Time vs Frequency domain.
   - Mesh generation.

2. Describe two widespread high-order methods using unstructured grids (FEM and DGM).

3. Discuss the computational cost and the sources of numerical error.

Choice of the physical model

Different sets of equations can be used for the acoustic propagation depending on

- The nature of the underlying mean flow
- The required level of approximation

Two main approaches

- Direct approaches (LES, DNS)
- Hybrid approaches (using acoustic analogy)

Direct approaches consider all scales of the problem

- Prohibitively expensive for most engineering applications

Discussed in previous lectures!

Lighthill's equation

Exact combination of the compressible Navier-Stokes equations

$$\frac{\partial^2 \rho'}{\partial t^2} - c_\infty^2 \nabla^2 \rho' = \frac{\partial^2 T_{i,j}}{\partial x_i x_j}$$

$\rightarrow$ Sound propagation modeled by the standard sound wave equation

$\rightarrow$ Lighthill stress tensor $T_{i,j} = \rho u_i u_j + (p' - c_\infty^2 \rho') - \tau_{i,j}$

- $\rho u_i u_j$: Reynolds stresses - non-linear effects $\rightarrow$ turbulent flows
- $p' - c_\infty^2 \rho'$: non-isentropic effects $\rightarrow$ unsteady heat source (combustion)
- $\tau_{i,j}$ describes viscosity effects (often negligible)

Discussed in previous lectures!

Physical models: levels of approximation

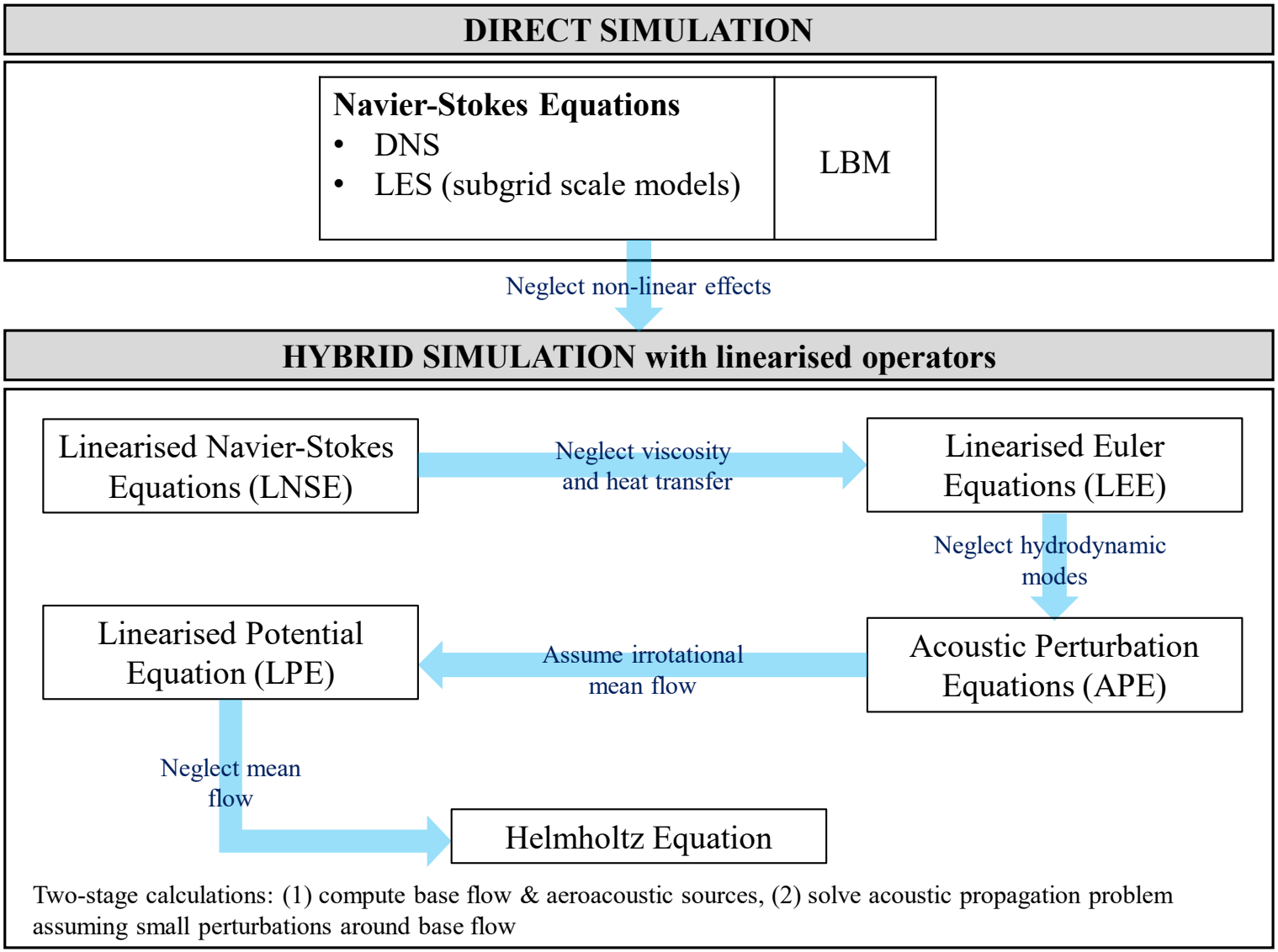

Two-stage calculations: (1) compute base flow & aeroacoustic sources, (2) solve acoustic propagation problem assuming small perturbations around base flow

Linearized Euler Equations

In 2D Cartesian coordinates, LEEs in conservative form read as:

$$\frac{\partial \boldsymbol{q}'}{\partial t} + \frac{\partial \mathbf{A}_x \boldsymbol{q}'}{\partial x} + \frac{\partial \mathbf{B}_y \boldsymbol{q}'}{\partial y} = \mathbf{0}, \tag{1}$$

where $\boldsymbol{q}' = [\rho', (\rho u)', (\rho v)', p_c']^T$ is the unknown vector, $p_c = (p/p_\infty)^{1/\gamma}$ is the non-dimensional pressure Goldstein, 2001, p_∞ is a reference pressure, γ is the specific heat ratio. The flux matrices are defined as follows:

$$\mathbf{A}_x = \begin{bmatrix} 0 & 1 & 0 & 0 \\ -u_0^2 & 2u_0 & 0 & \dfrac{\rho_0 c_0^2}{p_{c_0}} \\ -u_0 v_0 & v_0 & u_0 & 0 \\ -\dfrac{p_{c_0}}{\rho_0} u_0 & \dfrac{p_{c_0}}{\rho_0} & 0 & u_0 \end{bmatrix} \quad \text{and} \quad \mathbf{B}_y = \begin{bmatrix} 0 & 0 & 1 & 0 \\ -u_0 v_0 & v_0 & u_0 & 0 \\ -v_0^2 & 0 & 2v_0 & \dfrac{\rho_0 c_0^2}{p_{c_0}} \\ -\dfrac{p_{c_0}}{\rho_0} v_0 & 0 & \dfrac{p_{c_0}}{\rho_0} & v_0 \end{bmatrix}.$$

Assuming $\boldsymbol{q}'(\boldsymbol{x}, t) = \boldsymbol{q}'(\boldsymbol{x}, \omega) \mathrm{e}^{\mathrm{i}\omega t}$, Equations (1) in the frequency domain read:

$$\mathrm{i}\omega \boldsymbol{q}' + \frac{\partial \mathbf{A}_x \boldsymbol{q}'}{\partial x} + \frac{\partial \mathbf{B}_y \boldsymbol{q}'}{\partial y} = \mathbf{0}\,. \tag{2}$$

where ω is the angular frequency.

Monopole source in uniform flow - LEE solution

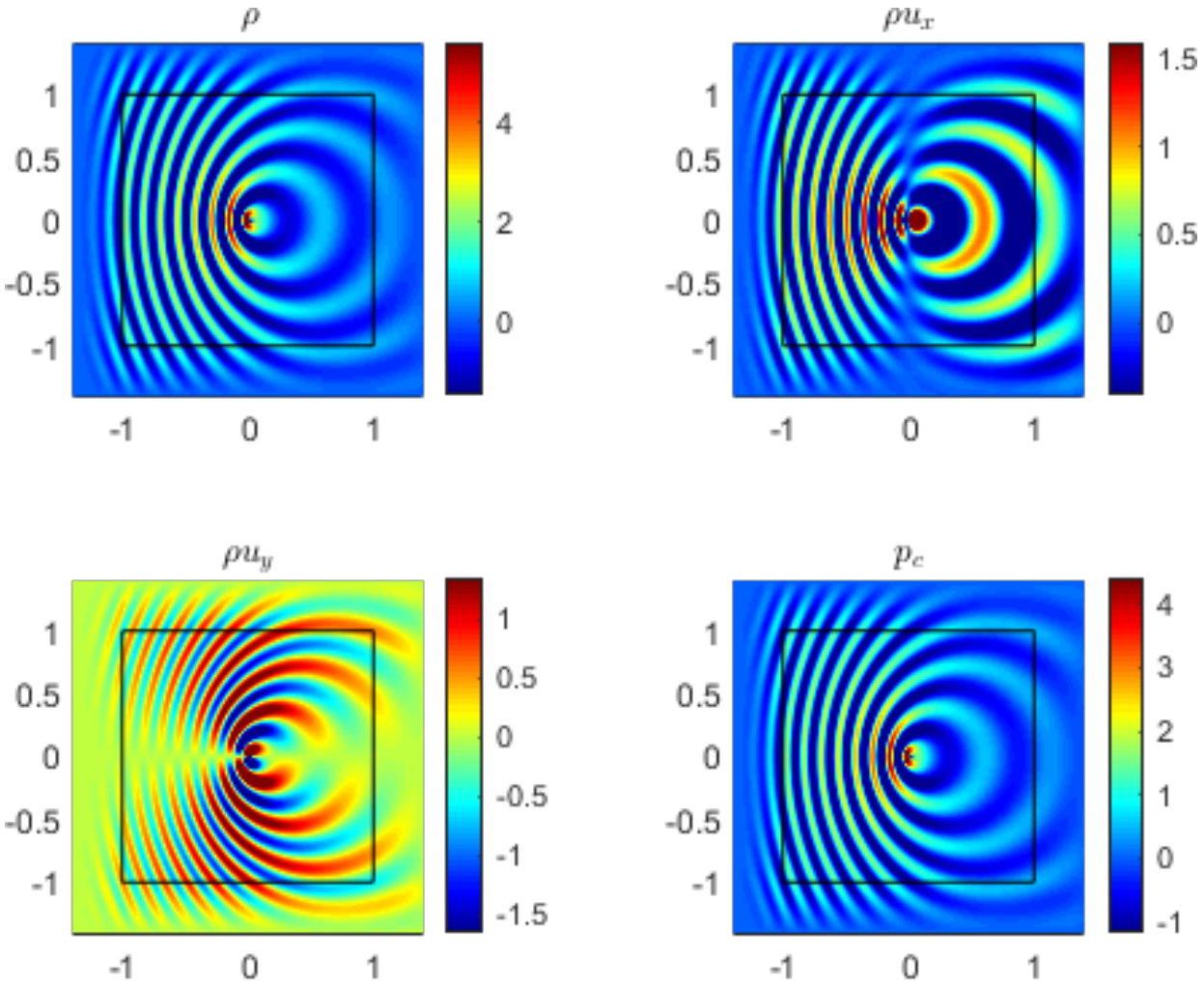

Figure: LEE results ($p = 4$) on the monopole source ($q_c = 1$) in x-oriented uniform flow $M = 0.6$ at $\omega = 18.48$.

Dipole source in uniform flow - LEE solution

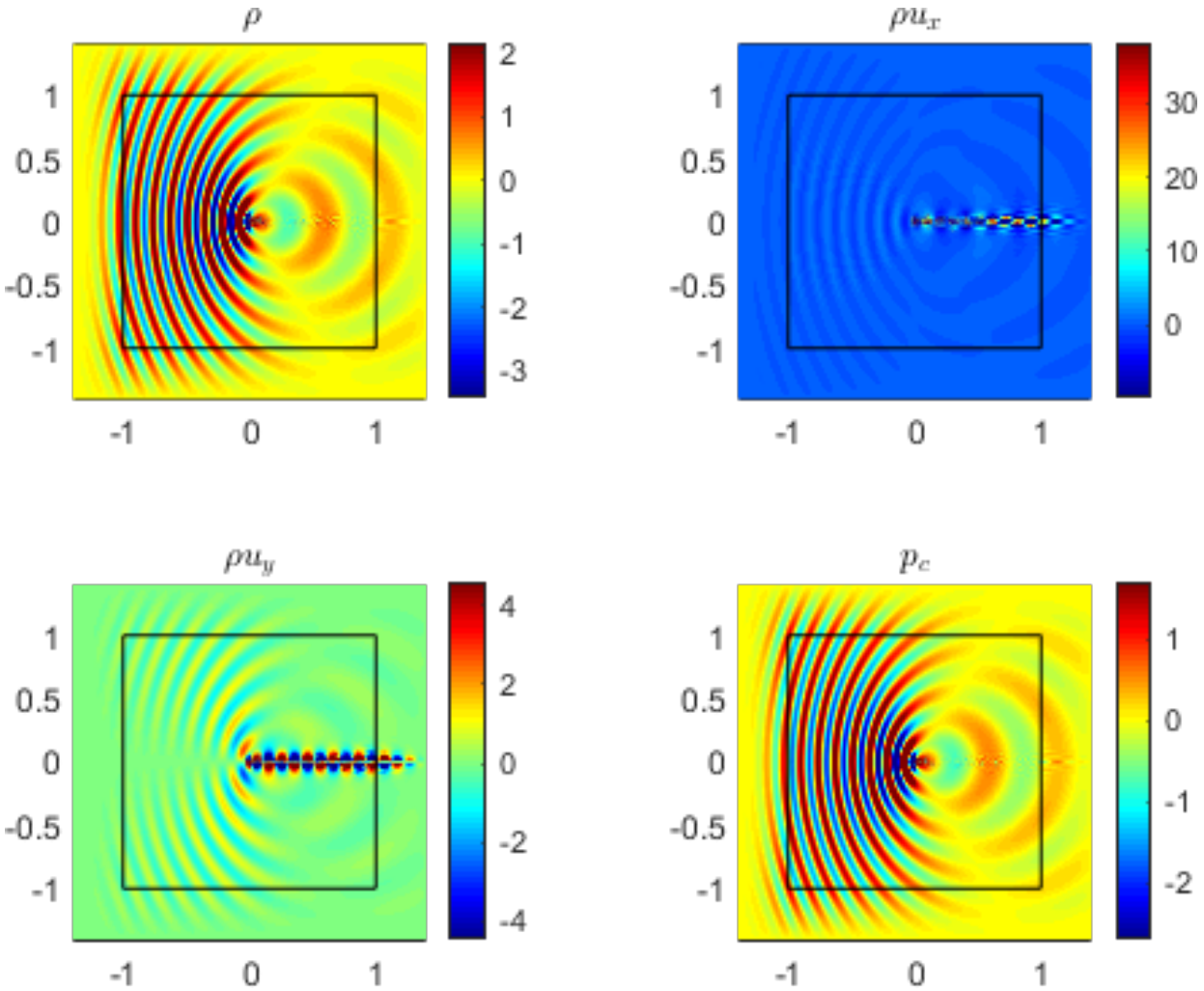

Figure: LEE results ($p = 4$) on the dipole source ($q_c = 1$) in x-oriented uniform flow $M = 0.6$ at $\omega = 18.48$.

Acoustic, hydrodynamic and entropy waves

As previously mentioned, the LEE support acoustic, hydrodynamic and entropy waves. In two dimensions, their dispersion relations read (Goldstein, 1976):

$$\boldsymbol{k}_{\mathrm{a,h,e}} = k_{\mathrm{a,h,e}} \begin{pmatrix} \cos\theta_{\mathrm{w}} \\ \sin\theta_{\mathrm{w}} \end{pmatrix} \text{ with}$$

$$k_{\mathrm{a}} = \frac{k_0}{1 + M_0 \cos(\theta_{\mathrm{w}} - \theta_0)} \text{ and}$$

$$k_{\mathrm{h}} = k_{\mathrm{e}} = \frac{k_0}{M_0 \cos(\theta_{\mathrm{w}} - \theta_0)} \,,$$

where $\boldsymbol{k}$ is the wavenumber vector, θ_{w} designates the plane wave orientation and $k_0 = \omega/c_0$. The direction and velocity of the mean flow are given by the angle θ_0 and the Mach number $M_0 = |\boldsymbol{u}_0|/c_0$. Note that the entropy and hydrodynamic waves, which are purely convected, are ruled by the same dispersion relation.

Acoustic, hydrodynamic and entropy waves

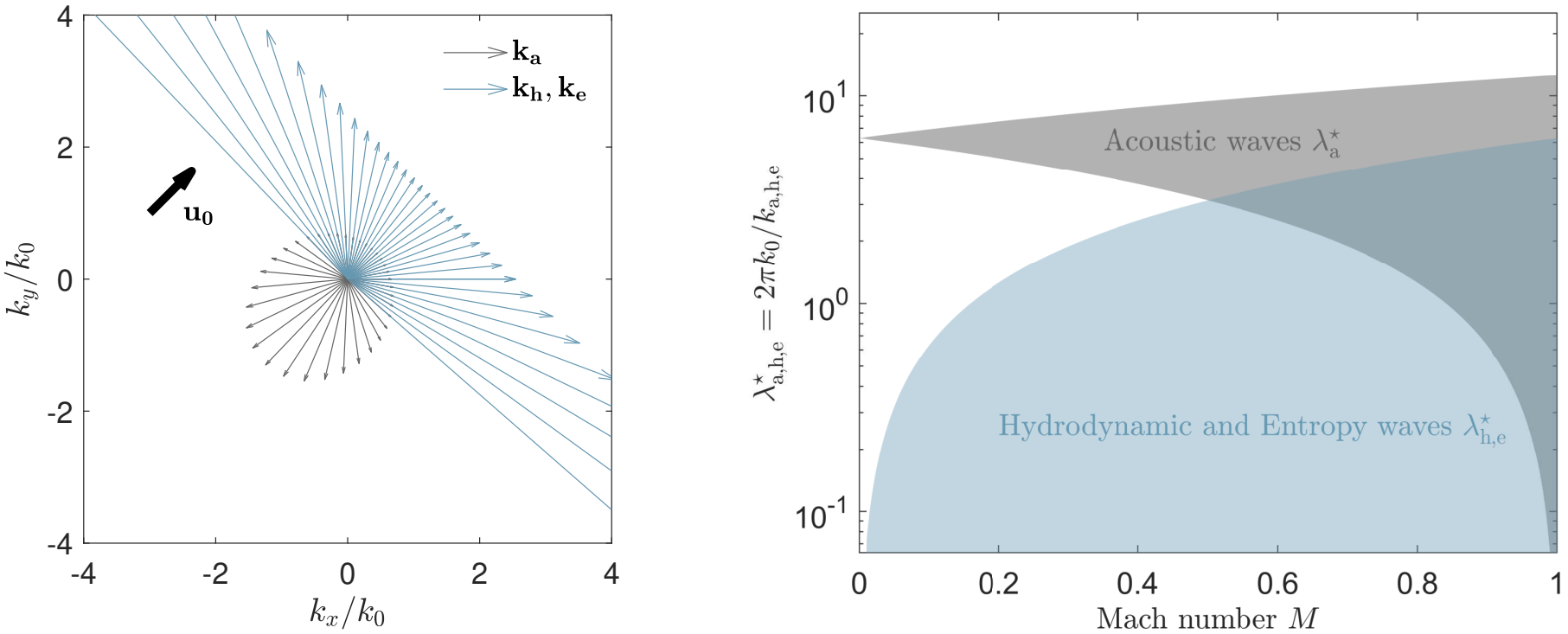

(a) Wave vectors at $M_0 = 0.5$, $\theta_0 = \pi/4$

(b) LEE normalized length scales

Figure: Illustration of the different dispersion relations supported by the LEE model. Acoustic (gray) and hydrodynamic/entropy (turquoise) wave vectors for a given Mach number M_0 (left), and range of normalized length scales as a function of the Mach number (right).

Gust on thin plate example

Uniform flow in direction x at $M = 0.3$

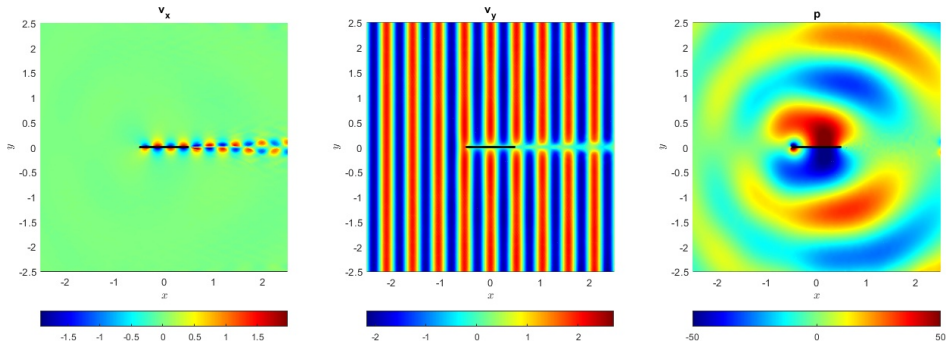

Real part of u_x (left), u_y (middle) and p (right)

Uniform flow in direction x at $M = 0.5$

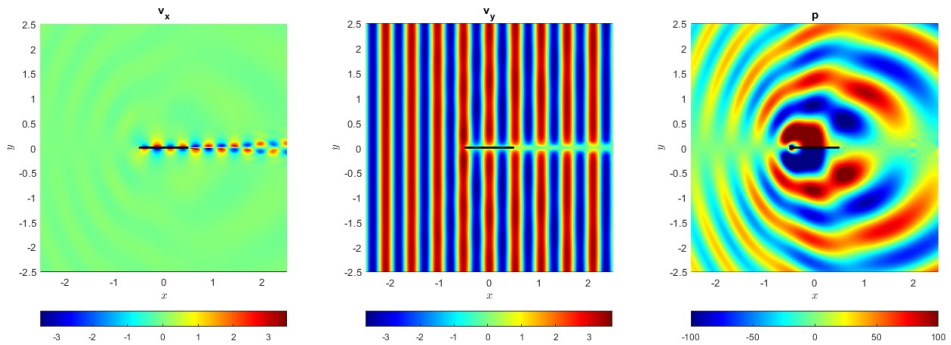

Real part of u_x (left), u_y (middle) and p (right)

Kelvin-Helmholtz instabilities

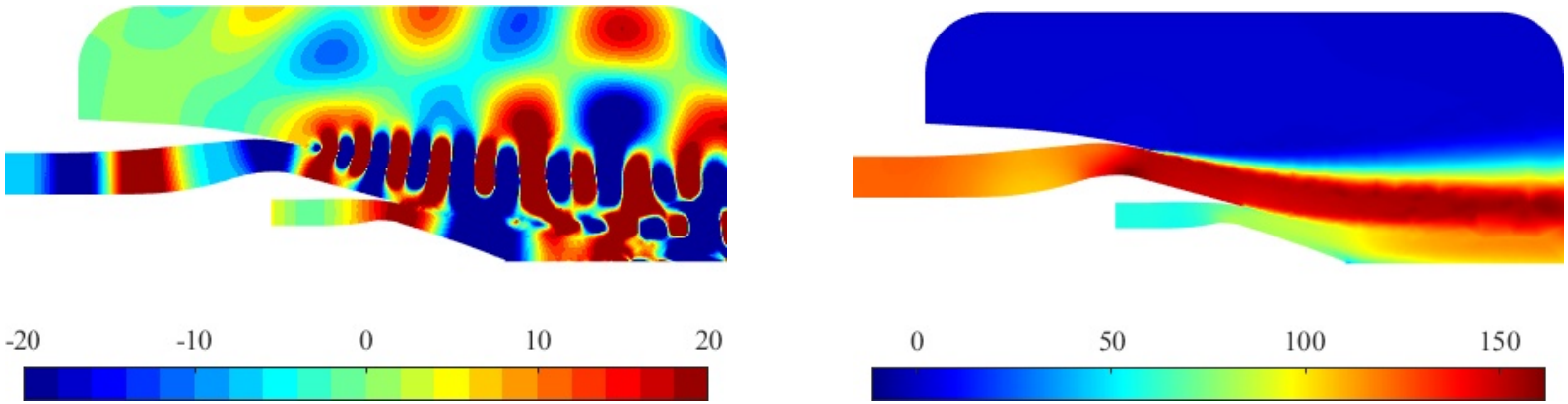

(a) LEE solution at 2082 Hz

(b) Axial mean flow

Figure: Illustration of the KH-instability on a LEE solution representing sound refraction through a hot jet exhaust (Turnex case).

- LEE suffers from KH-instabilities in parallel sheared flows (mostly at low frequency)
- Limitation of the physical model (absence of non-linearities and viscous terms)
- Affects both time and frequency domain solutions
- Different strategies were proposed (mean flow gradient suppression, APE, etc...)

Application of linear acoustic operators: monopole source in flow

Case #1: Uniform flow in direction x at $M = 0.6$

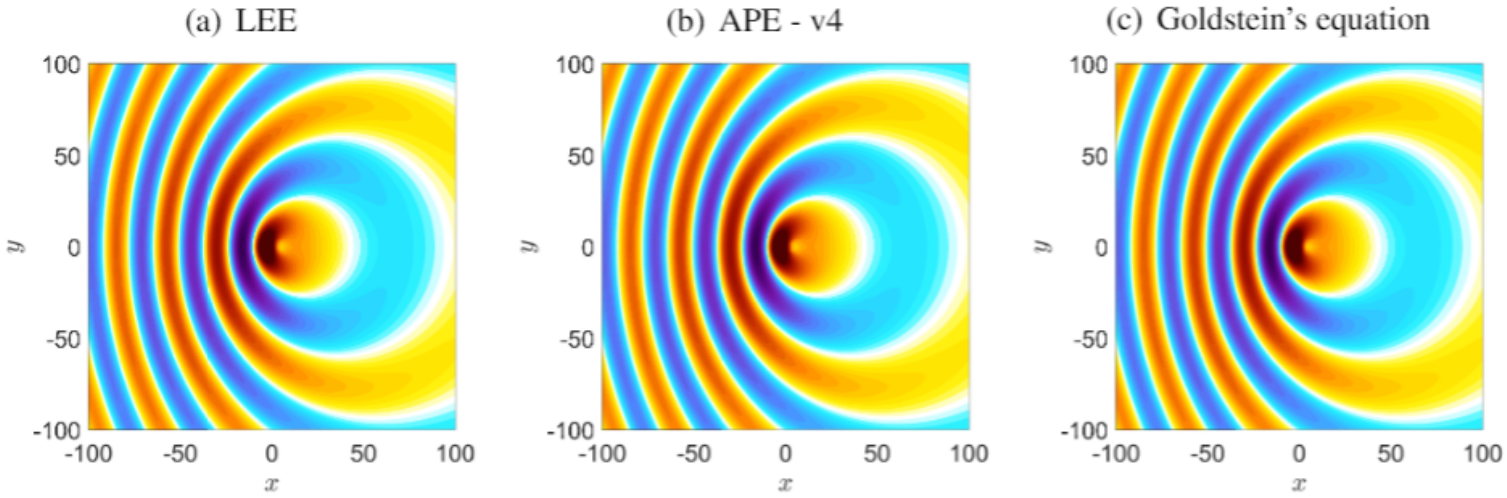

Real part of the acoustic pressure

- All operators are "equivalent" in uniform flows
- LEE and APE are vector-valued operators
- APE (Goldstein's equation) is a scalar operator (acoustic velocity potential)

Application of linear acoustic operators: monopole source in flow

Case #2: Sheared isothermal flow in direction x at $M = 0.6$

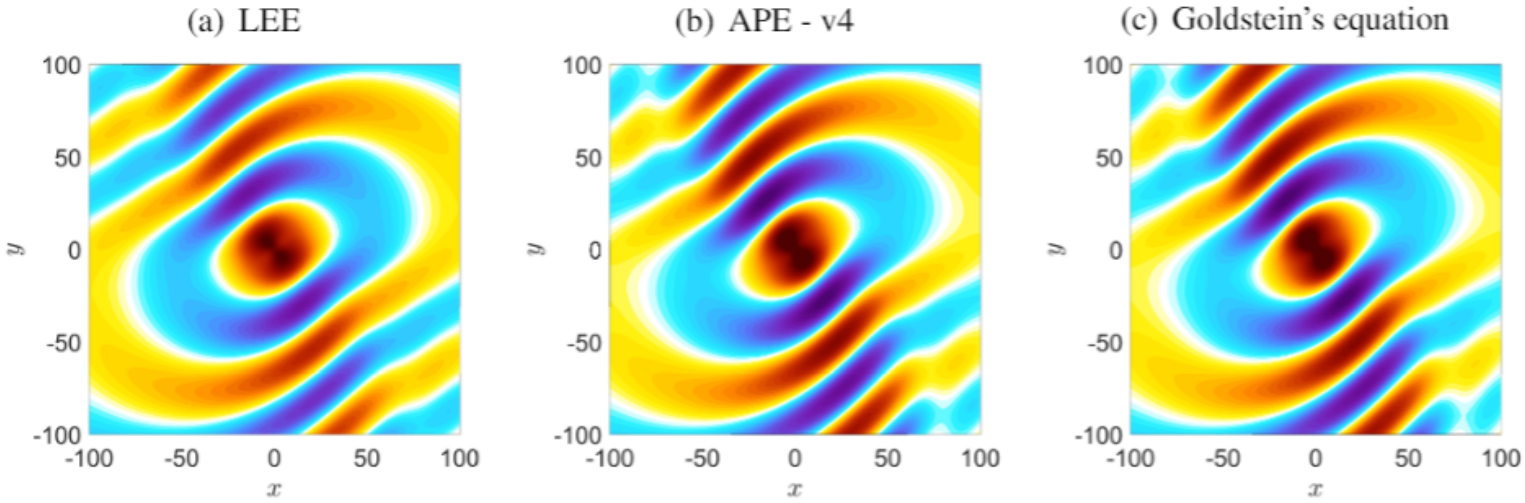

Real part of the acoustic pressure

- APE and LPE give "similar" results in sheared flows, they differ from the LEE
- Difference is usually acceptable in mildly sheared flows, higher in strongly sheared flows

Application of linear acoustic operators: monopole source in flow

Case #3: Hot jet flow in direction x at $M = 0.6$ (Spieser, 2020)

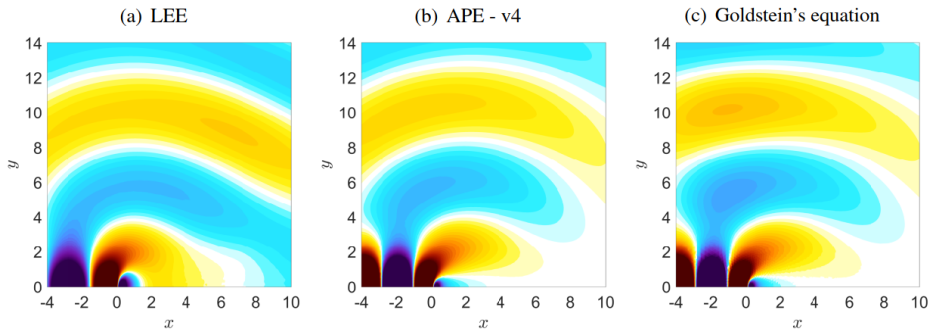

Strouhal number of 0.2

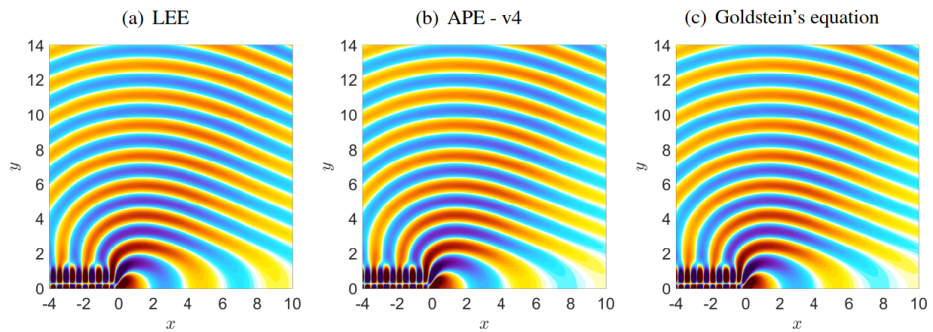

Strouhal number of 1

- Differences are usually emphasized in non-isothermal flows
- In any case, in the high frequency limit, APE and LPE converge to the LEE solution

Frequency vs time domain

Frequency domain:

- Well suited for tonal noise, linear problems, but can be used for frequency sweeps.
- Considered a way to avoid instabilities.
- Solutions are globally coupled $\Rightarrow$ Large memory requirements
- Do not scale well with problem size
- Multiple loads

Time domain:

- Well suited for broadband noise
- Non linear problems
- Issues with linear instabilities + impedance modeling
- Good scalability with problem size
- Single loading

Structured vs. Unstructured

Structured methods:

- Easier to achieve high accuracy (low dispersion, low dissipation).
- Simpler data structures that lead to better optimization and usage of computational resources (especially for vector processors and GPUs).
- Designing grids for complex geometries is time consuming and requires care to maintain grid quality.

Unstructured methods:

- Less user time needed to prepare model (although preparing a CAD geometry for a mesh generator can be tricky).
- Potential for automated mesh generation is greater (important for design optimization).
- More complex data structures, making it more difficult to maximise usage of computational resources.

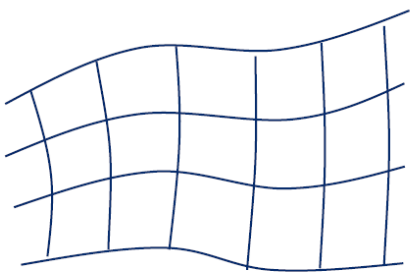

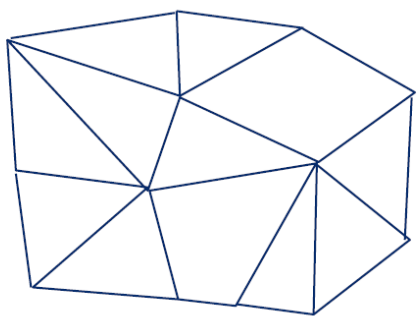

Numerical Methods

- Finite Difference Method
- Finite elements
- Discontinuous Galerkin method
- Boundary elements
- ...

	Complex geometries	Non-homogeneous media	High-order accurate	Conservation laws	Elliptic problems
FDM		✓	✓	✓	✓
FEM	✓	✓	✓	(✓)	✓
DGM	✓	✓	✓	✓	(✓)
BEM	✓		(✓)		✓

Table: Generic properties of usual methods used in acoustics and aero-acoustics. The brackets indicate that the method can be used if suitable adaptations are made, but that it is not the most intuitive approach.

Far-field boundary conditions

Efficient absorbing conditions allow to reduce the computational cost.

- infinite elements (IFEM) (Astley, 2000)
- absorbing boundary conditions (ABC) (Engquist and Majda, 1977)
- Perfectly Matched Layers (PML) (Bécache et al., 2003)

PML is the most common technique nowadays

- coordinate stretching (complex coordinates)
- propagating waves are analytically continued into exponentially decaying ones
- Automatic formulation for any domain of convex shape (AML) (Bériot and Modave, 2020)
- For transient wave propagation, need for auxiliary variables (Modave et al., 2017).
- With flow, unstabilities appear and Lorentz transformation is required (Hu, 2008; Marchner et al., 2020).

Automatically Matched Layer (AML)

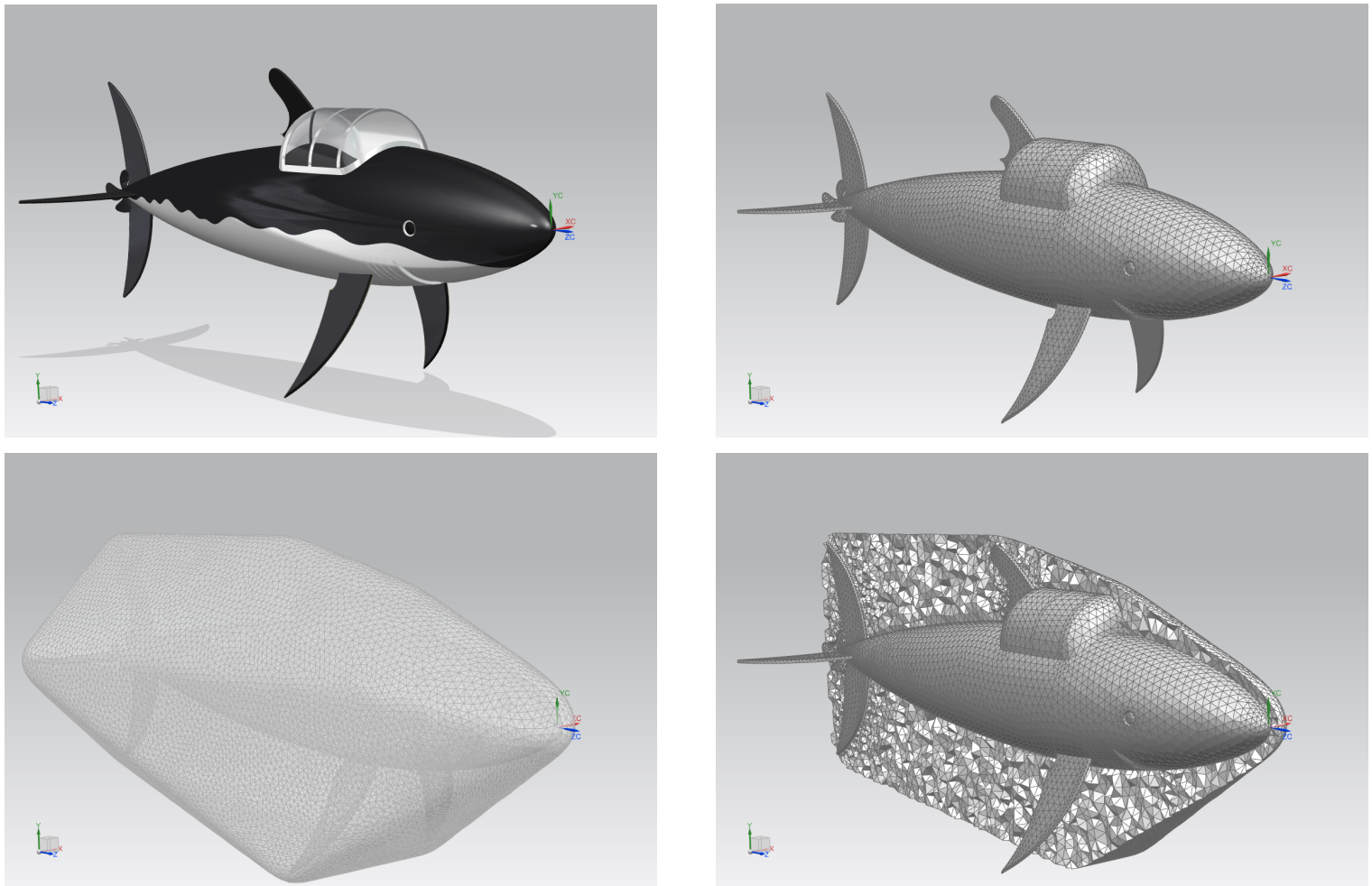

Figure: CAD model *(top left)*, surface mesh *(top right)*, convex exterior surface *(bottom left)* and cut view of tetrahedral mesh *(bottom right)*, from Bériot and Modave (2020)

Automatically Matched Layer (AML)

- Minimizes the size of the computational domain
- Automatic extrusion of the PML, no user input required

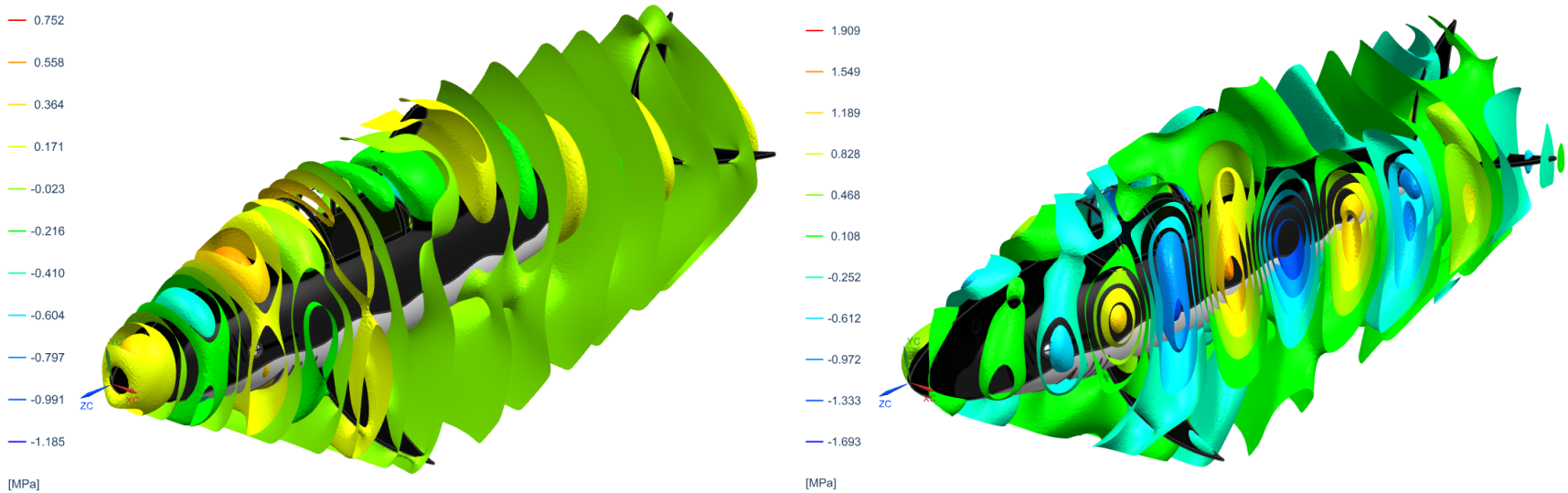

(a) Incidence $(0, 0, -1)$

(b) Incidence $(0, 1, -1)$

Figure: Real part of the scattered fields obtained in the physical domain for both incident fields, from Bériot and Modave (2020)

Mesh generation

Main algorithms (Frey and George, 2010):

- Advancing front methods.
- Delaunay triangulations.
- Tree decomposition: octree, quadtree...

Features:

- Conformal vs non-conformal meshes (hanging nodes).
- Anisotropic (boundary layers, shocks...).
- Hybrid meshes (combine different types of elements).

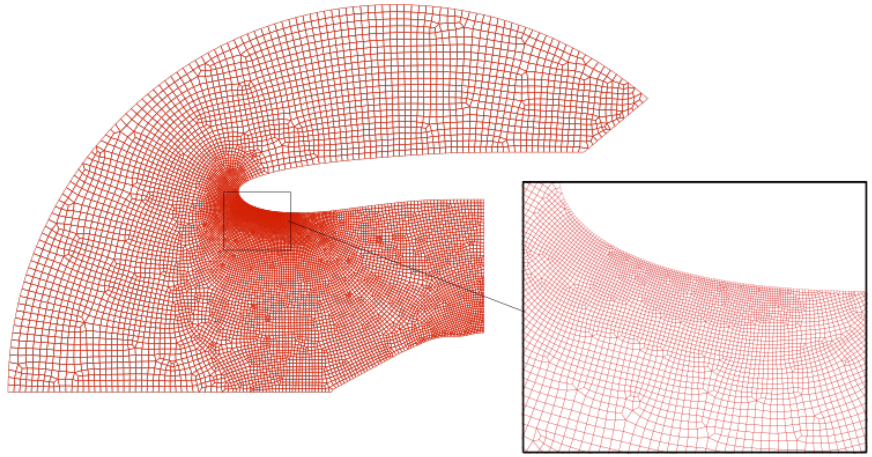

From Astley et al. (2002).

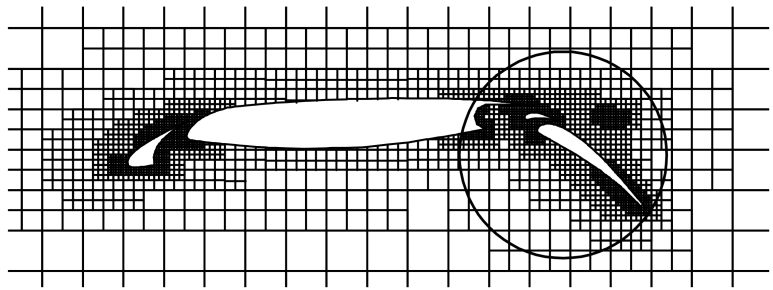

From Sang and Shi (2013).

Mesh generation

Mesh resolution:

- 'Rule of thumb' for resolution of geometry, base flow, and solution.
- *A priori* error estimator: control the generation of the mesh.
- Adaptive Mesh Refinement (AMR): iteratively adjust the mesh based on *a posteriori* error estimators to achieve a prescribed tolerance.

Isogeometric approach:

- Use of CAD constructs (NURBS) to approximate the solution.
- The objective is to bypass the mesh generation.
- See Hughes et al. (2005).

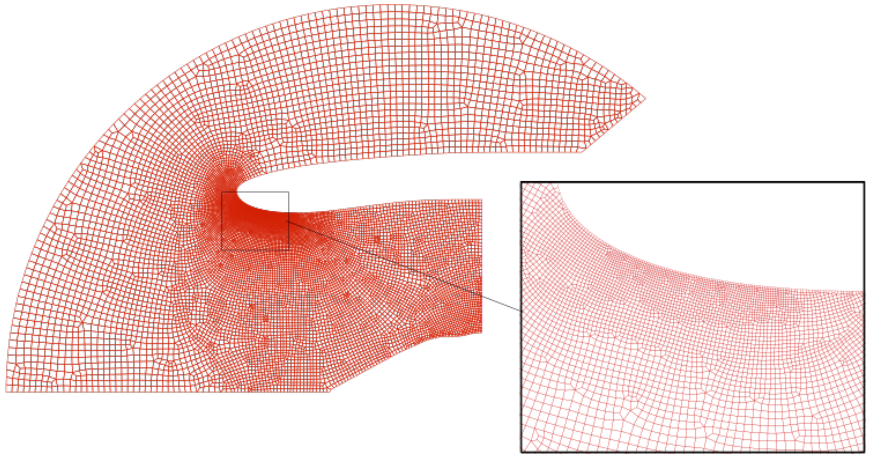

From Astley et al. (2002).

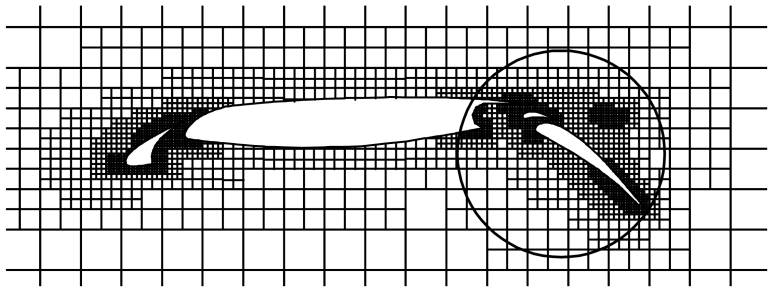

From Sang and Shi (2013).

A Frequency-Domain Finite Element Method

FEM: linearised potential theory

- Consider the propagation of small perturbations over a known steady base flow.
- Assume that the perturbations and the base flow are potential:

$$\mathbf{u} = \mathbf{u}_0 + \mathbf{u}' \,, \quad \text{with } \mathbf{u}_0 = \boldsymbol{\nabla}\phi_0 \,, \quad \mathbf{u}' = \boldsymbol{\nabla}\phi' \,. \tag{3}$$

  The scalar functions $\phi_0(\mathbf{x})$ and $\phi'(\mathbf{x}, t)$ are the velocity potentials.
- Inviscid and homentropic base flow and perturbations.

Linear wave equation for the acoustic potential (Eversman, 1991):

$$\frac{\partial}{\partial t}\left(-\frac{\rho_0}{c_0^2}\frac{\mathrm{D}_0\phi'}{\mathrm{D}t}\right) + \boldsymbol{\nabla}\cdot\left(\rho_0\boldsymbol{\nabla}\phi' - \frac{\rho_0}{c_0^2}\frac{\mathrm{D}_0\phi'}{\mathrm{D}t}\mathbf{u}_0\right) = 0 \,, \tag{4}$$

where $\mathrm{D}_0/\mathrm{D}t = \partial/\partial t + \mathbf{u}_0\cdot\boldsymbol{\nabla}$ is the material derivative in the base flow.

- This model is cheaper to solve than the Linearised Euler Equations (only 1 unknown instead of 4 or 5).
- In use in several commercial simulation codes: Siemens Simcenter Acoustics, Actran TM, Comsol.

FEM: formulation

- Assume time-harmonic solutions with $\phi \sim \mathrm{e}^{+\mathrm{i}\omega t}$.
- Weighted residual formulation (Ritz–Galerkin method) over a domain Ω:

$$\int_\Omega \overline{\psi} \left[\mathrm{i}\omega \left(\frac{\rho_0}{c_0^2} \frac{\mathrm{D}_0 \phi'}{\mathrm{D}t} \right) - \boldsymbol{\nabla} \cdot \left(\rho_0 \boldsymbol{\nabla} \phi' - \frac{\rho_0 \mathbf{u}_0}{c_0^2} \frac{\mathrm{D}_0 \phi'}{\mathrm{D}t} \right) \right] \mathrm{d}\Omega = 0 \,, \quad \forall \psi \,, \tag{5}$$

  with ψ the test function and $\overline{\ }$ the complex conjugate.
- The corresponding weak variational formulation (assuming continuous solutions):

$$\int_\Omega \rho_0 \overline{\boldsymbol{\nabla} \psi} \cdot \boldsymbol{\nabla} \phi' - \frac{\rho_0}{c_0^2} \overline{\frac{\mathrm{D}_0 \psi}{\mathrm{D}t}} \frac{\mathrm{D}_0 \phi'}{\mathrm{D}t} \, \mathrm{d}\Omega + \int_{\partial\Omega} \overline{\psi} \frac{\rho_0}{c_0^2} \frac{\mathrm{D}_0 \phi'}{\mathrm{D}t} \mathbf{u}_0 \cdot \mathbf{n} - \overline{\psi} \rho_0 \frac{\partial \phi'}{\partial n} \, \mathrm{d}S = 0 \,. \tag{6}$$

- The boundary integral is modified to include the boundary conditions...

FEM: examples of boundary conditions

- **Solid surface:** The surface is impervious to the mean flow ($\mathbf{u}_0 \cdot \mathbf{n} = 0$) and with a prescribed normal velocity V_n the boundary integral becomes

$$\int_{\partial\Omega} (-\rho_0 \overline{\psi} V_n) \, \mathrm{d}S \, ,$$

  and is part of the right-hand side.
- **Duct modes BC**
- **Non-reflecting BC** (PML, Infinite Elements)

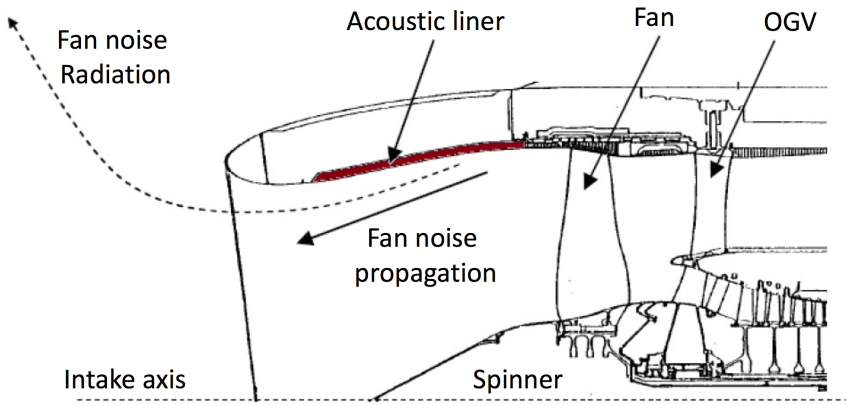

From Mustafi (2013).

Impedance condition: The boundary condition derived by Myers (1980) describes a locally reacting liner with impedance $Z(\omega)$ underneath an infinitely thin boundary layer.

$$\frac{\partial \phi'}{\partial n} = \frac{-\rho_0}{\mathrm{i}\omega Z}\left(\frac{\mathrm{D}_0}{\mathrm{D}t} - \mathbf{n}\cdot\frac{\partial \mathbf{u}_0}{\partial n}\right)\frac{\mathrm{D}_0\phi'}{\mathrm{D}t}\ . \tag{7}$$

- Eversman (2001) provides a detailed discussion of the implementation of this condition in FE models.
- This is currently the standard way of describing liners in this model, but the assumption of an infinitely thin boundary layer can lead to inaccurate predictions.

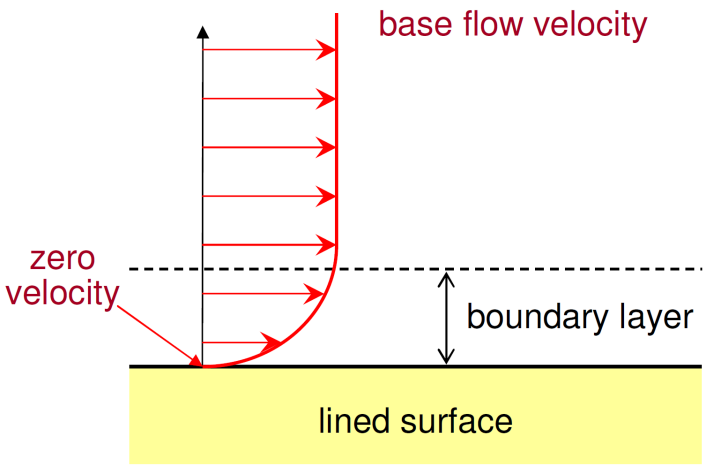

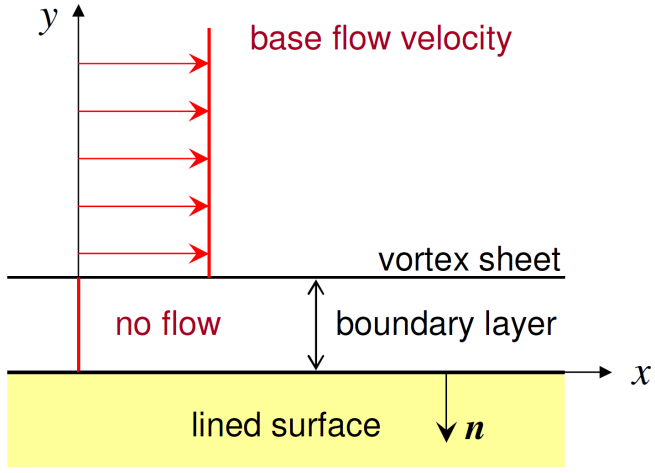

FEM: discrete model

- The solution ϕ' and test function ψ are discretised using shape functions...

$$\phi'(\mathbf{x}) = \sum_n \phi_n S_n(\mathbf{x}) \; . \tag{8}$$

We have reduced the problem to a finite number of degrees of freedom ϕ_n.

- The element matrices are calculated e.g.

$$(\mathbf{A})_{mn} = \int_\Omega \rho_0 \overline{\boldsymbol{\nabla} S_m} \cdot \boldsymbol{\nabla} S_n - \frac{\rho_0}{c_0^2} \overline{\frac{\mathrm{D}_0 S_m}{\mathrm{D}t}} \frac{\mathrm{D}_0 S_n}{\mathrm{D}t} \, \mathrm{d}\Omega \; . \tag{9}$$

Numerical integration methods are used for this.

- Assembly of element matrices to form the global, sparse system of equations.
- Direct or iterative solvers...

FEM: shape functions

- Typically linear, and quadratic Lagrange shape functions
- High-order finite elements yield significant benefits in performance.
- H^1-conforming hierarchic polynomials allows for locally nonuniform distribution of the order across the mesh
- This makes them suitable candidates for p- and hp-adaptivity (Šolín et al., 2003).
- Non-isoparametric approach (geometry and field interpolation are different)

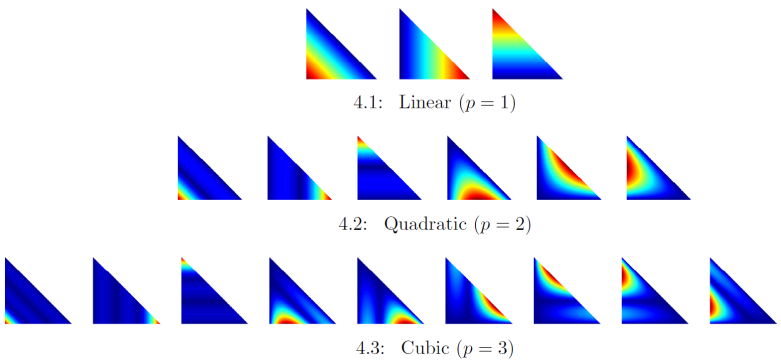

4.1: Linear ($p = 1$)

4.2: Quadratic ($p = 2$)

4.3: Cubic ($p = 3$)

Lagrange shape functions

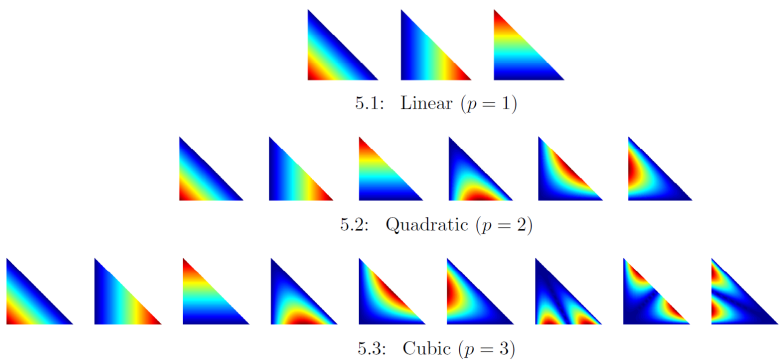

5.1: Linear ($p = 1$)

5.2: Quadratic ($p = 2$)

5.3: Cubic ($p = 3$)

Hierarchic shape functions

Lobatto shape functions

- Also referred to as **integrated Legendre**
- $p + 1$ shape functions on line element
- $(p + 1)^2$ shape functions on quad element (tensor product)
- Vertex, edge and bubble shape functions (latter can be statically condensed during assembly)

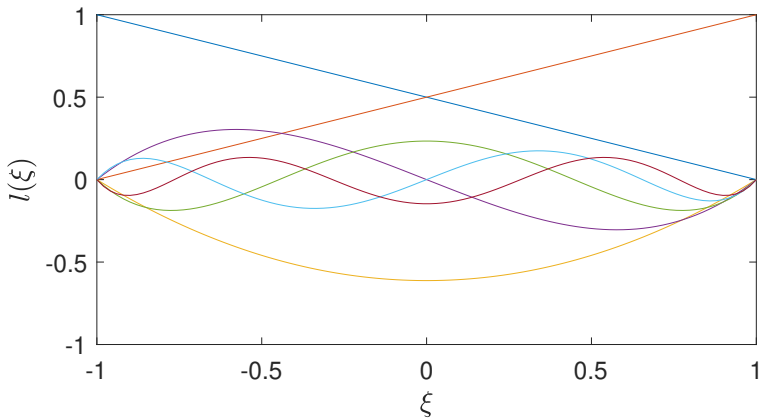

(a) Line, up to $p = 5$

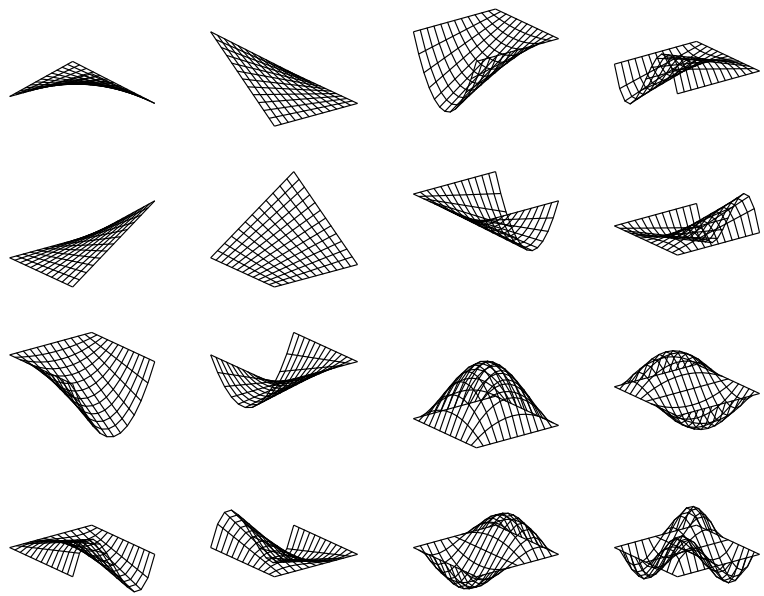

(b) Quad, up to $p = 3$

Sparse system solvers

Direct solvers:

Gaussian elimination is equivalent to:

$$\mathbf{A} = \mathbf{LU}$$

Initial system $\mathbf{LUx} = \mathbf{b}$ and solved in two steps,

$$\mathbf{Ly} = \mathbf{b}, \quad \mathbf{Ux} = \mathbf{y}.$$

- Multi-frontal solvers for LU or Cholesky factorizations.
- Memory requirements are very high. Poor scaling with problem size.
- Typical solvers: MUMPS and PARDISO
- 3 steps Analysis/Factorization/Solving
- Partitioning and re-numbering are critical.

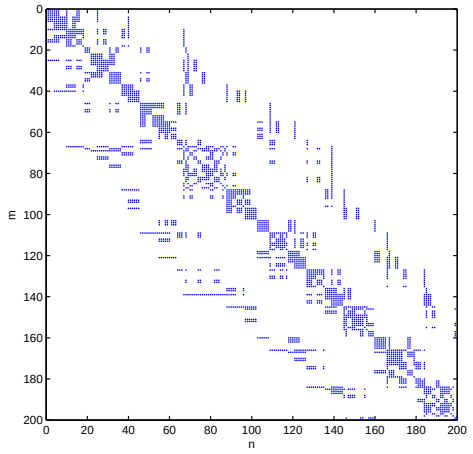

Iterative solvers:

- Better scaling with problem size than direct solvers.
- But efficiency highly dependent on preconditioner (Ernst and Gander, 2012), and convergence is not always guaranteed.
- Common approaches: multi-grid methods, Krylov solvers (Vorst, 2003).

Numerical Accuracy

Sources of numerical error

There are multiple sources of error in a numerical model, e.g.:

- Geometry error
- Flow/BCs interpolation errors
- Spatial discretization error
- Time discretization error
- Buffer zone or Non reflecting condition error
- ...

and there is a "competition" between them.

Geometry

Geometry:

- Necessary to represent the relevant geometrical features without introducing spurious scattering.
- Typically use of linear or quadratic elements to describe the geometry.

Example: propagation of a single duct mode in a circular duct (Rarata, 2014).

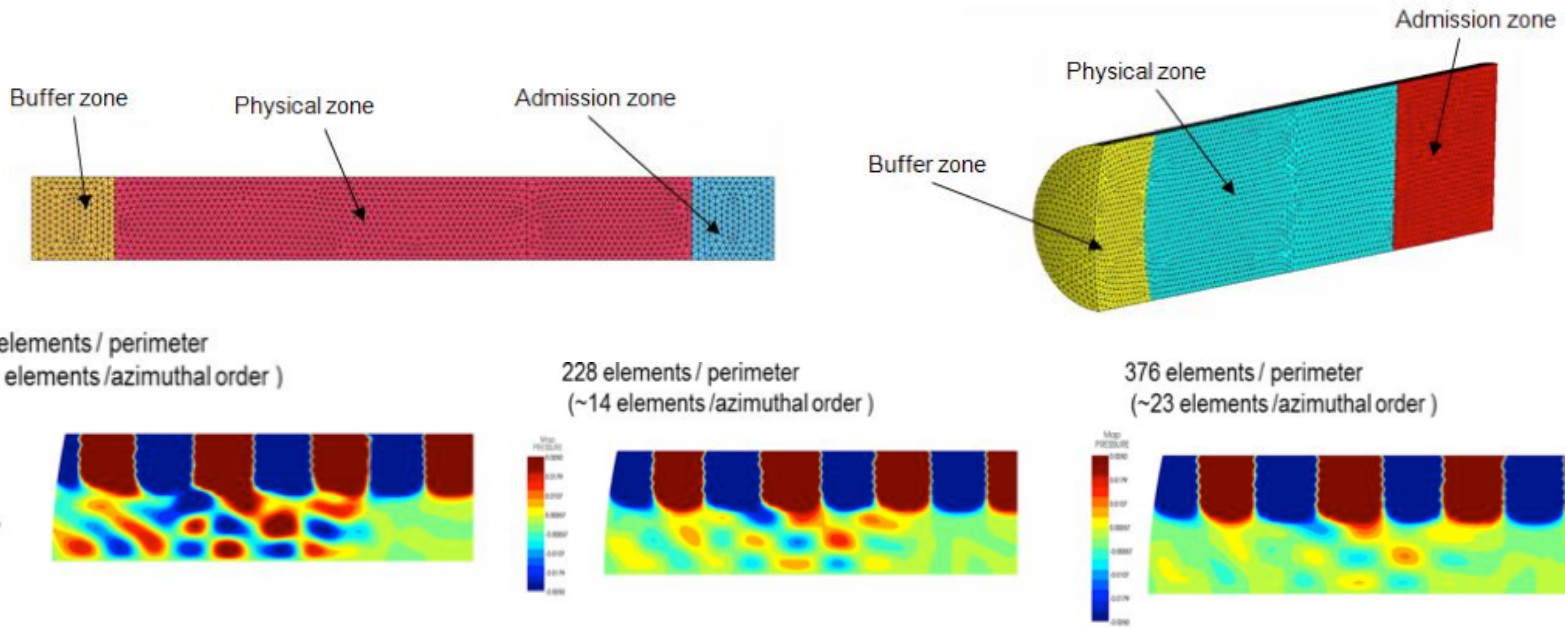

Base flow

Mean flow interpolation:

- Interpolating the mean flow can introduce significant errors.
- In particular in regions with strong gradients (shear layers, boundary layers).

Illustration: Exact hyperbolic tangent shear layer (left) and its linear interpolation on a coarse acoustic mesh (right).

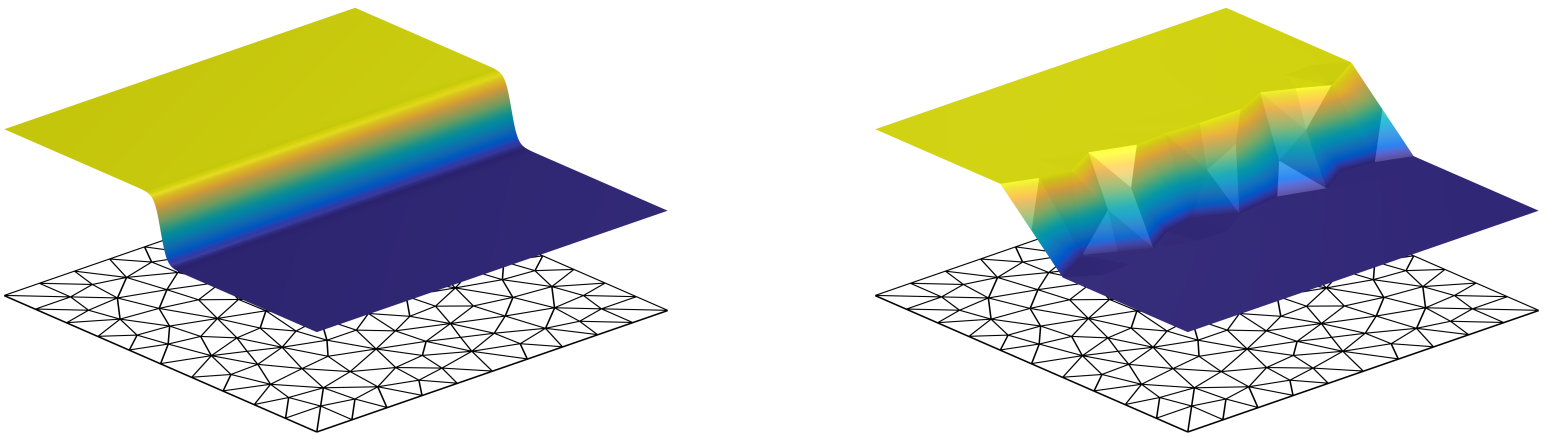

Numerical error

As an example, the following error bound was derived for the *hp*-FEM for the Helmholtz equation (Ihlenburg and Babuška, 1997):

$$E < C_1 \left(\frac{kh}{2p} \right)^p + C_2 kL \left(\frac{kh}{2p} \right)^{2p} . \quad (10)$$

- Wavenumber k, element size h and polynomial order p.
- The number of elements per wavelength is $2\pi/(kh)$.
- Algebraic convergence with mesh resolution (h-refinement).
- Exponential convergence with interpolation order p (p-refinement).

Relative H^1 error for the p-FEM in 1D from Bériot et al. (2013).

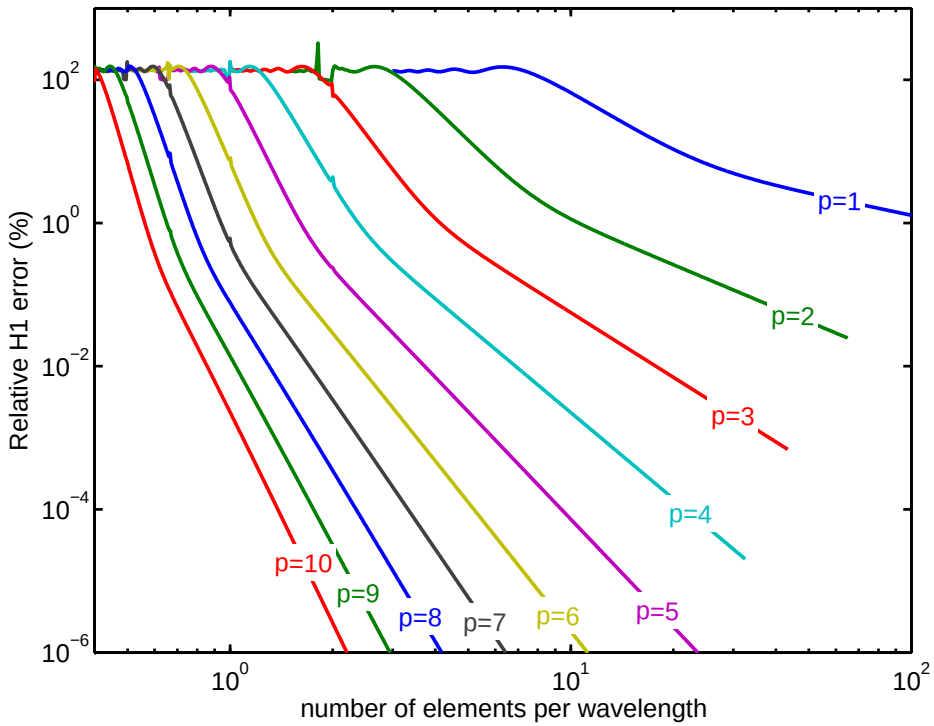

See Bayliss et al. (1985), Ihlenburg and Babuška (1995), Ihlenburg and Babuška (1997) and Ihlenburg (1998).

Numerical error

The numerical error can be decomposed into different sources:

$$E < C_1 \left(\frac{kh}{2p}\right)^{p} + C_2 kL \left(\frac{kh}{2p}\right)^{2p}. \quad (11)$$

- Interpolation error dominates at high resolution.
- Dispersion error and 'Pollution effect' dominate at low resolution.
- Disclaimer 1: this is only valid for smooth solutions.
- Disclaimer 2: this error estimate is too conservative for the dispersion error for high orders.

Relative H^1 error for the p-FEM in 1D from Bériot et al. (2013).

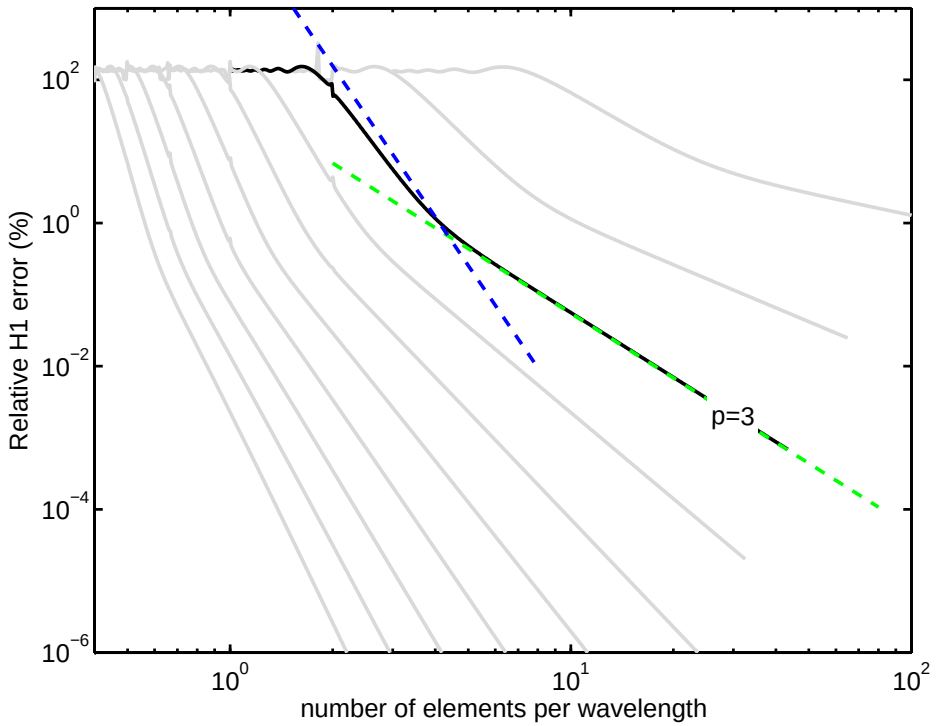

Interpolation error

- The interpolation error controls the asymptotic behaviour of the numerical error.
- It scales like $(kh)^p$ for the H^1 error or $(kh)^{p+1}$ for the L^2 error.
- It can be controlled by keeping the mesh resolution constant (kh constant).
- *Quasi-optimal methods*: actual solution is close to the best interpolation available.
- *Consistent interpolation*: the interpolation error $\to 0$ when $h \to 0$ or p increases.

Comparison of linear and quadratic interpolations.

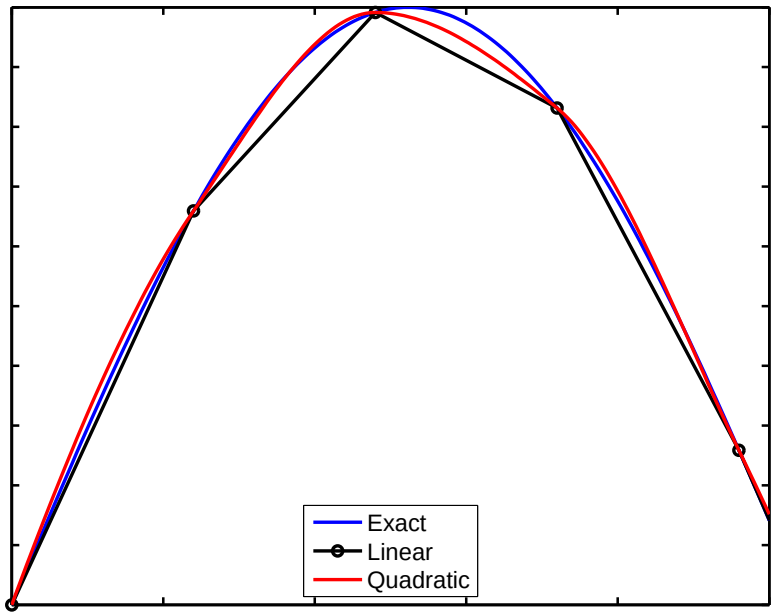

Dispersion error

The dispersion error is the difference between exact wavenumber k and the actual wavenumber $\tilde{k}$ observed in the numerical model (for a fixed frequency ω).

We can measure the error on

- The wavenumber k.
- The phase velocity ω/k.
- The group velocity $\partial\omega/\partial k$.

For *hp*-FEM Ainsworth (2004a) provides the following expression for the relative dispersion error (with $kh \ll 1$):

$$\frac{\tilde{k}-k}{k} \simeq -\frac{1}{2}\left[\frac{p!}{(2p)!}\right]^2 \frac{(kh)^{2p}}{2p+1} + \mathcal{O}((kh)^{2p+2}) \,. \tag{12}$$

- The dispersion error is controlled by the mesh resolution (keeping kh constant).
- It tends to dominate for relatively low resolution.
- In this case no diffusion, only dispersion ($\tilde{k}$ is real).
- For the effect of the mean flow see Bériot et al. (2013).

Pollution effect

- Dispersion error is local (it is error introduced over a single wavelength).
- Phase delay and dissipation build up as the wave propagates through the computational domain.
- This effect scales with the number of wavelength in the domain $kL/(2\pi)$.
- Keeping the number of elements per wavelength constant is *not* sufficient to control the global error (the famous 'rule of thumb' of 8 points per wavelength is not valid).
- Increasing the order p reduces the relative significance of the pollution effect.

Propagation of a simple wave with 1% dispersion error (exact, numerical)

Small domain (L^2 error: 5.2%)

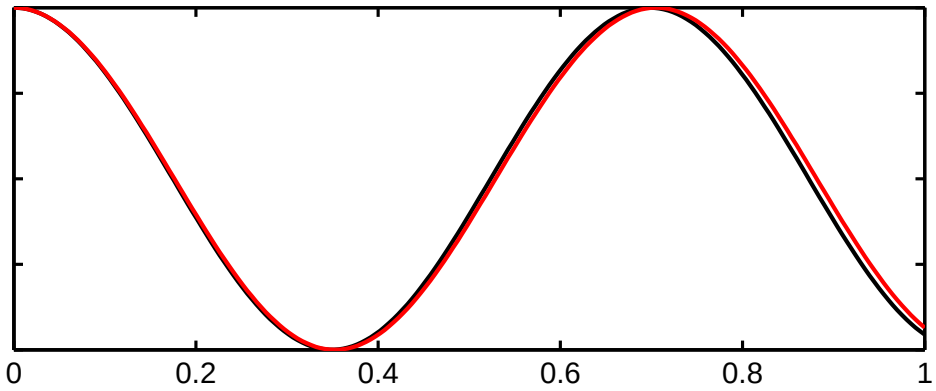

Large domain (L^2 error: 51%)

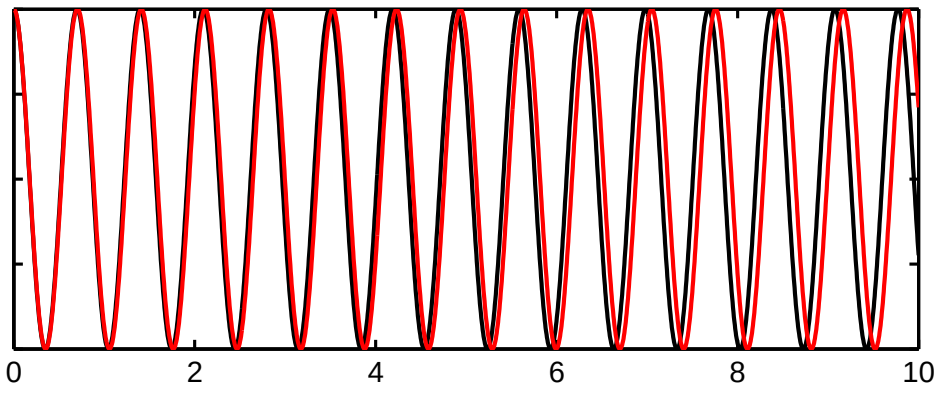

Adaptive high-order FEM

Motivations

In many acoustic applications $\Rightarrow$ wide frequency range (i.e. from 20 Hz to 20 kHz):

- Spans orders of magnitude in wavelength scales!
- Model preparation difficult (one mesh per frequency?)
- Instead, common to use **a single mesh** (most refined) $\Rightarrow$ expensive!

In Bériot et al. (2016) new approach proposed based on **adaptive high-order FEM**

- A single input mesh is used
- Order is automatically defined before each frequency (*a priori* indicator)
- Aeroacoustic applications first explored in Gabard et al. (2018)
- Later extended to anisotropic (directional) orders in (Bériot and Gabard, 2019)

p-FEM adaptive approach - toy problem

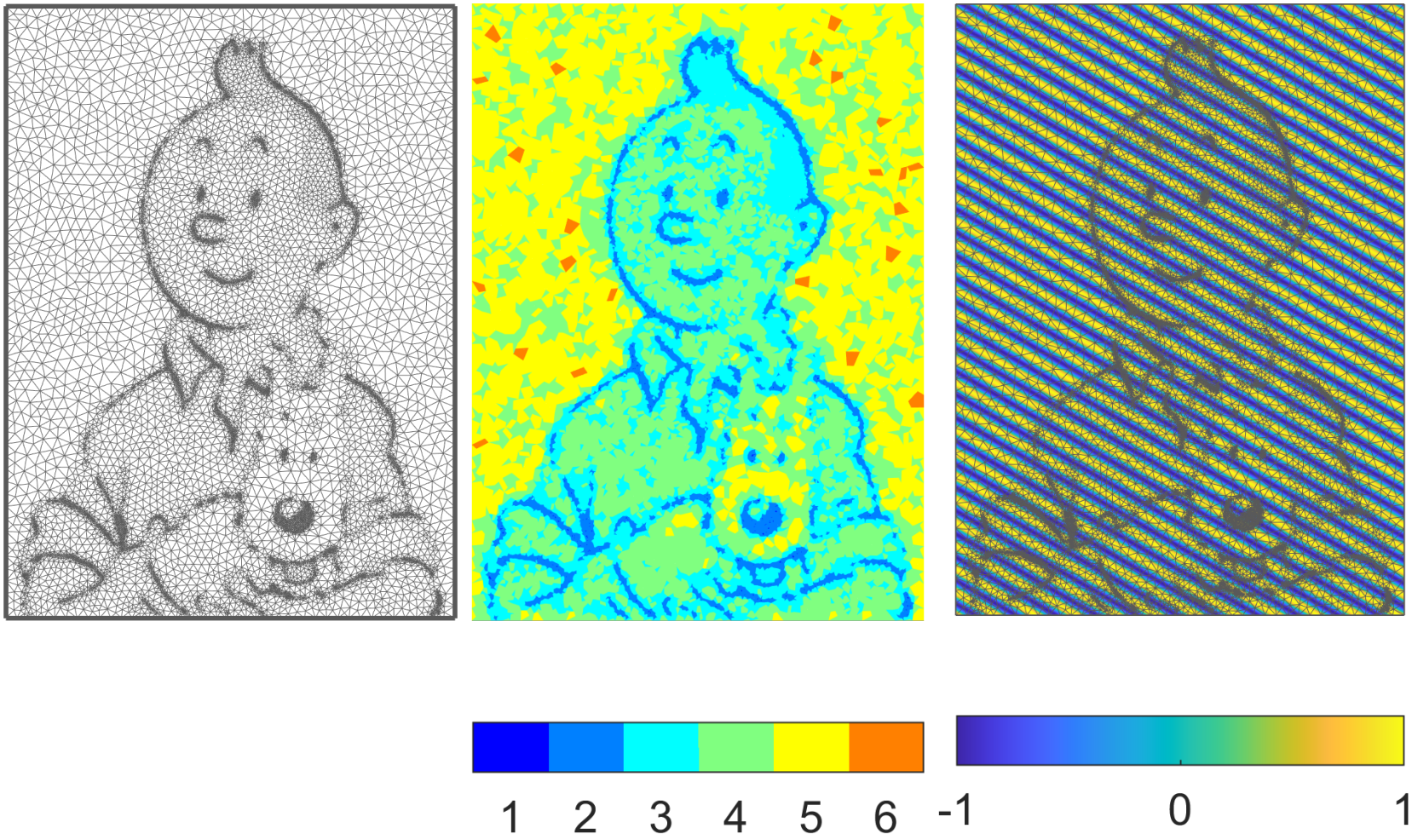

Figure: Error indicator determines automatically the order distribution (middle from $p = 1$ to $p = 6$) before the calculation based on the frequency ($\omega = 140$) and a user defined error target (here $E_T = 1\%$). The actual L^2 error is of 0.78%.

p-FEM adaptive approach - toy problem

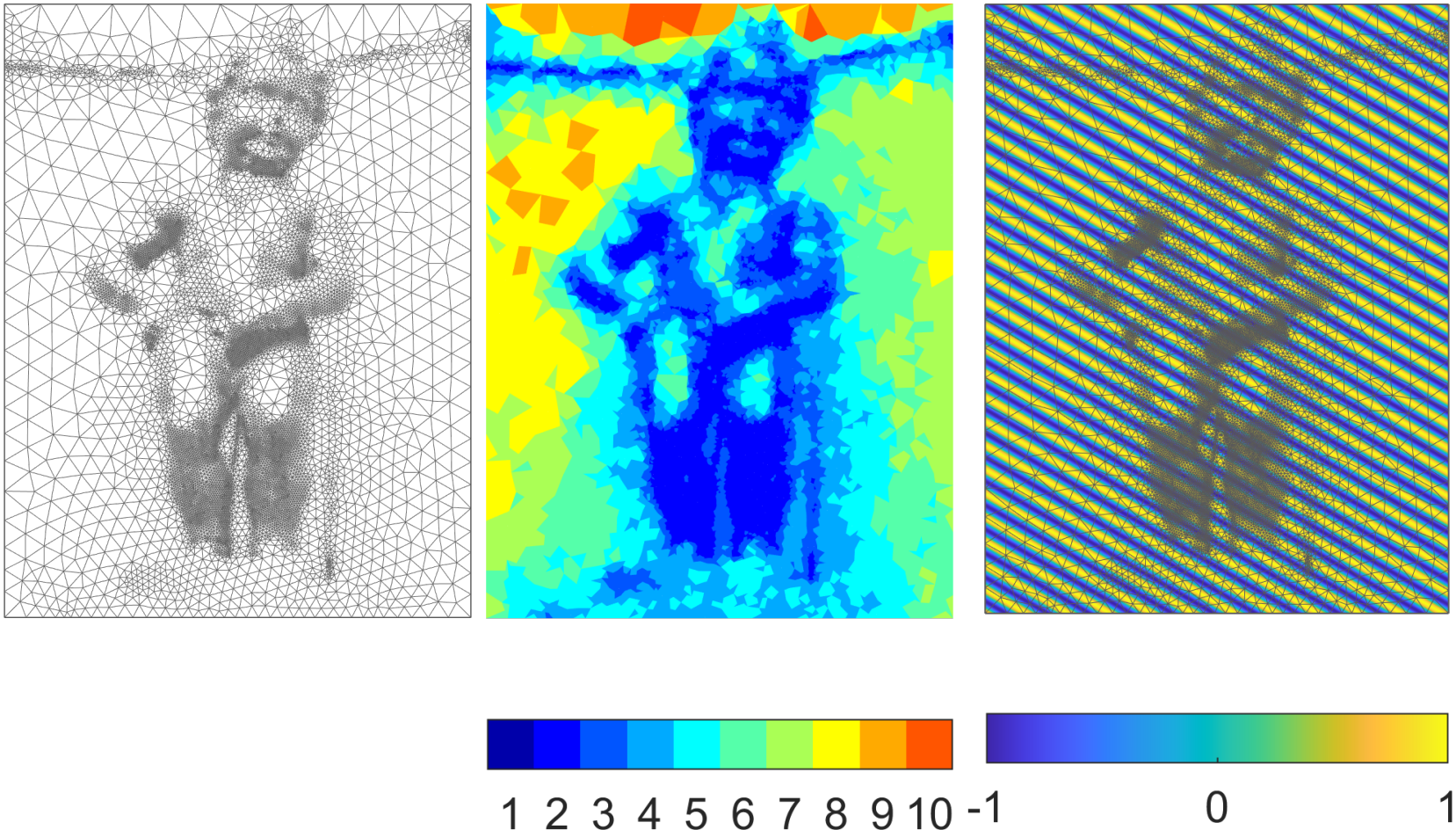

Figure: Error indicator determines automatically the order distribution (middle from $p = 1$ to $p = 10$) before the calculation based on the frequency ($\omega = 140$) and a user defined error target (here $E_T = 1\%$). The actual L^2 error is of 0.84%.

p-FEM adaptive - how does it work?

Edge orders are assigned first - using an *a priori* error indicator

- Solving a 1D problem with same effective resolution, defined as:

$$(kh)_{e_i} = \max_{\xi \in [-1,+1]} 2k_{\max}(\xi)|\mathbf{t}(\xi)| \,, \quad \text{with } k_{\max}(\xi) = \max_{\theta_w \in [0,2\pi]} \mathbf{k}(\mathbf{x}(\xi), \theta_w) \cdot \frac{\mathbf{t}(\xi)}{|\mathbf{t}(\xi)|}$$

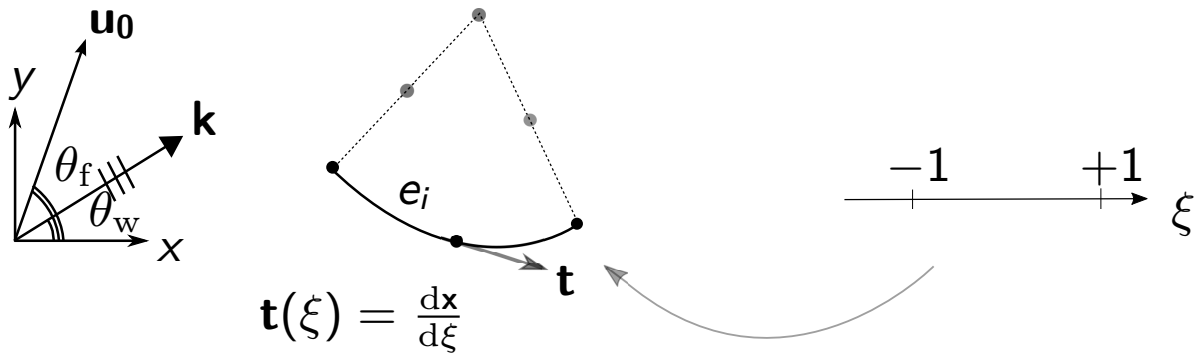

Figure: Illustration of the mapping from the reference space to the physical space used to define the edge order p^{e_i} on curved edge e_i, with information from the local fluid properties $(c_0, \mathbf{u}_0)$.

- Accounts for possible **flow non-uniformities** and **mesh curvature**

p-FEM adaptive - how does it work?

Directional face and solid (bubble) orders are assigned afterwards

- Using element-type dependent conformity rules

Hexahedron: $p_i^{b\xi} = \max\left(p_i^{e1}, p_i^{e3}, p_i^{e9}, p_i^{e11}\right)$ $p_i^{b\eta} = \max\left(p_i^{e2}, p_i^{e4}, p_i^{e10}, p_i^{e12}\right)$ $p_i^{b\zeta} = \max\left(p_i^{e5}, p_i^{e6}, p_i^{e7}, p_i^{e8}\right)$

Prism: $p_i^{b\xi} = \max\left(p_i^{e1}, p_i^{e2}, p_i^{e7}, p_i^{e8}\right)$ $p_i^{b\eta} = \max\left(p_i^{e2}, p_i^{e3}, p_i^{e8}, p_i^{e9}\right)$ $p_i^{b\zeta} = \max\left(p_i^{e4}, p_i^{e5}, p_i^{e6}\right)$

Tetrahedron: $p_i^{b\xi} = \max\left(p_i^{e1}, p_i^{e2}, p_i^{e5}\right)$ $p_i^{b\eta} = \max\left(p_i^{e2}, p_i^{e3}, p_i^{e6}\right)$ $p_i^{b\zeta} = \max\left(p_i^{e4}, p_i^{e5}, p_i^{e6}\right)$

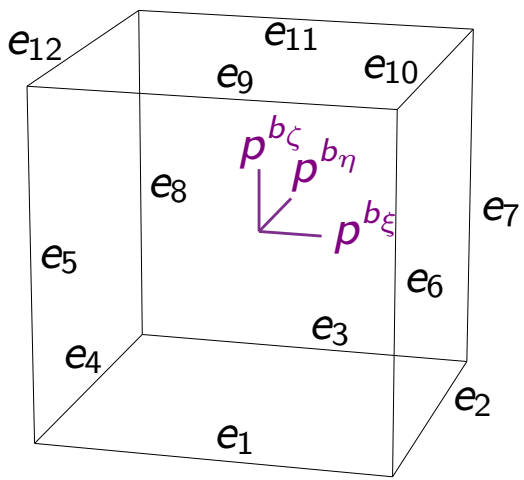

(a) Hexahedral element

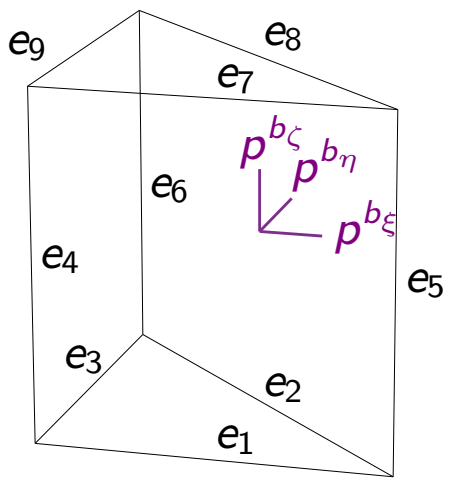

(b) Prism element

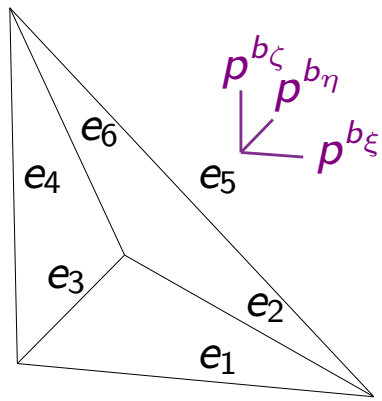

(c) Tetrahedral element

Figure: Edge number and local orientation convention for all element types, required for the definition of the solid anisotropic order conformity rules, $p^{b\xi}, p^{b\eta}, p^{b\zeta}$.

p-FEM adaptive - anisotropy for high-aspect ratio elements

Directional orders can be used (Bériot and Gabard, 2019)

- Useful for meshes with high aspect ratio elements

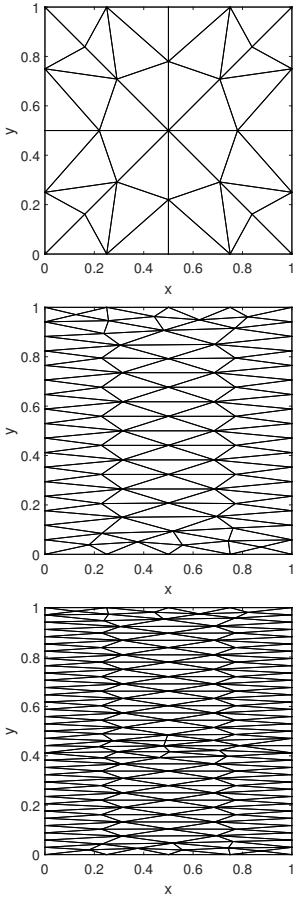

Figure: Triangular anisotropic meshes with element aspect ratio $\delta = 1$ (top), $\delta = 5$ (middle) and $\delta = 10$ (bottom).

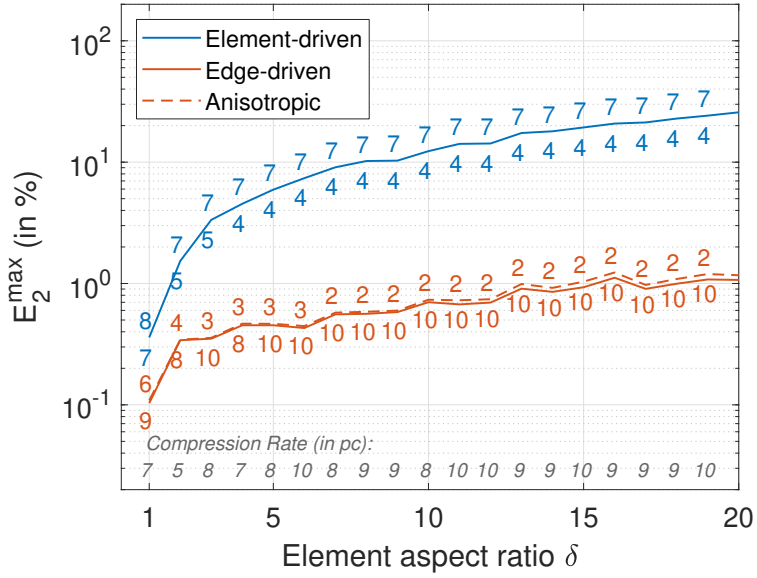

(a) Triangular mesh

Figure: Maximum L^2 error E_2^{max} at $\omega = 30$ with increasing element aspect ratio, from $\delta = 1$ to $\delta = 20$ for a target error of $E_T = 1\%$

p-FEM adaptive - anisotropy for high-aspect ratio elements

Directional orders can be used (Bériot and Gabard, 2019)

- Useful for meshes with high aspect ratio elements

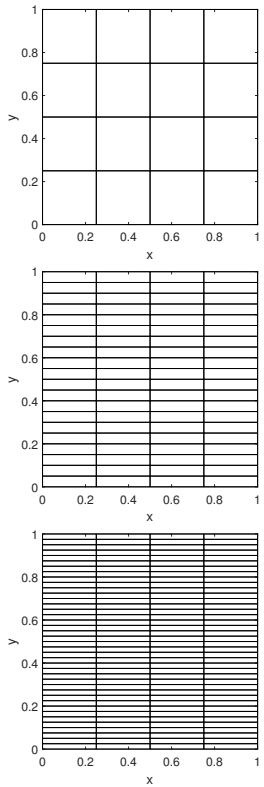

Figure: Quadrangular anisotropic meshes with element aspect ratio $\delta = 1$ (top), $\delta = 5$ (middle) and $\delta = 10$ (bottom).

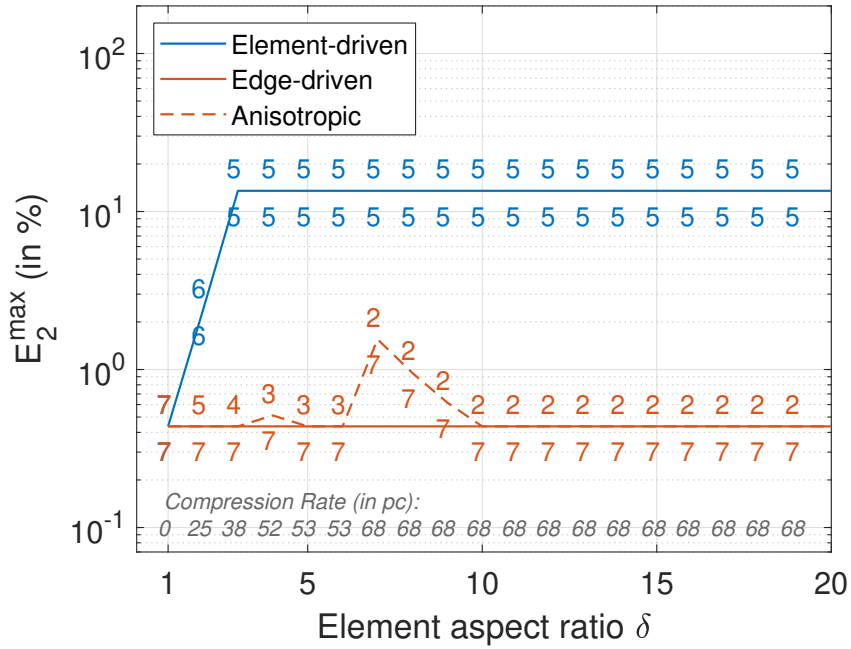

(a) Quadrangular mesh

Figure: Maximum L^2 error E_2^{max} at $\omega = 30$ with increasing element aspect ratio, from $\delta = 1$ to $\delta = 20$ for a target error of $E_T = 1\%$

p-FEM adaptive approach - anisotropy for flow applications

Directional orders can be used (Bériot and Gabard, 2019)

- Useful when the physics is anisotropic (flow acoustics)

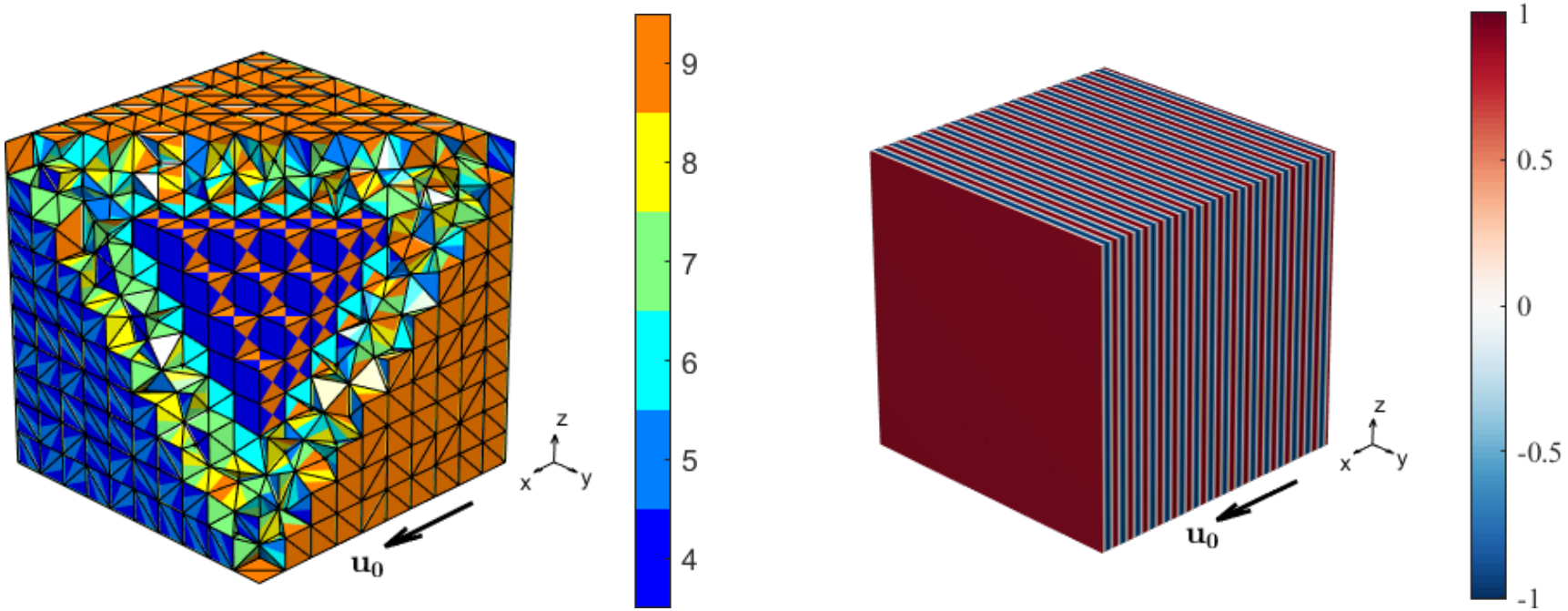

Figure: Anisotropic p-FEM approach from Bériot and Gabard (2019) for convected applications. Directional orders obtained from the error indicator (left) and upstream wave (right) at $\omega = 20$ with Mach number $M = 0.8$ - target accuracy $\varepsilon_T = 1\%$.

FEM: applications in aeroacoustics

FEM: applications in aeroacoustics

One application where FEM is routinely used in the industry: noise radiation from aircraft engines:

- Early attempts of using finite elements for noise radiation from engine intakes (Abrahamson, 1977; Sigman et al., 1978).
- Sound propagation in ducts using the linearized Euler equations solved with weighted residual or finite element methods (Eversman and Astley, 1981; Astley and Eversman, 1981).
- Modelling sound radiation (linearised potential theory):
  - Use of FEM and integral equations (Horowitz et al., 1986).
  - Wave envelope methods and infinite elements (Astley, 1985; Astley and Eversman, 1988).
- Development of commercial codes like SysNoise by LMS and then Actran-TM by FFT.
- Time-domain finite element formulation (Hamilton and Astley, 2005).
- Applications of the FEM to the linearised Euler equations (Rao and Morris, 2006; Iob et al., 2010).
- See reviews by Thompson (2006) and Astley (2009).

FEM: applications in aeroacoustics

- JT15D commercial engine
- Air intake radiation ($\varnothing$ 0.53m)
- static condition
- 5 operating conditions
- 28 blades, 41 rods installed
- generates a $(-13, 0)$ rotor locked mode

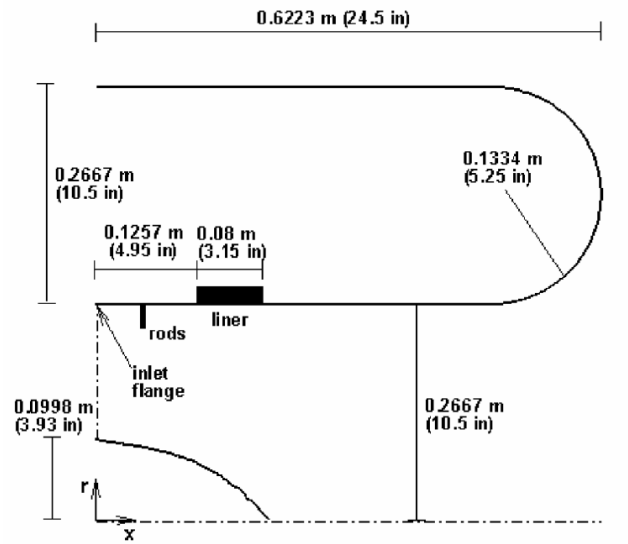

- Experimental results available (Lan et al., 2004)
- Numerical results (LEE) available (Lan et al., 2004)

FEM: applications in aeroacoustics

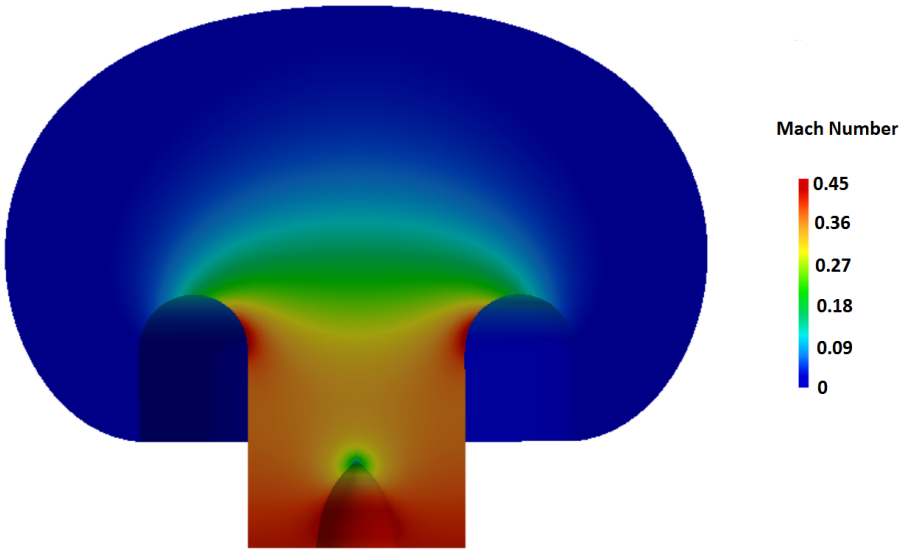

Mean flow calculation at 13500 RPM

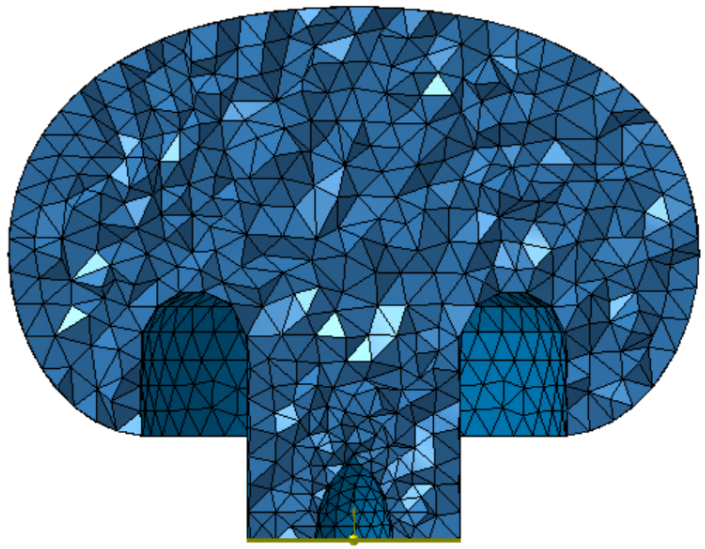

Tetrahedral parabolic (T10) mesh cross section

- Analytic source model (modal input)
- Steady potential mean flow.
- Propagation model: **linearized potential theory**

Computational model for the JT15D air intake test case.

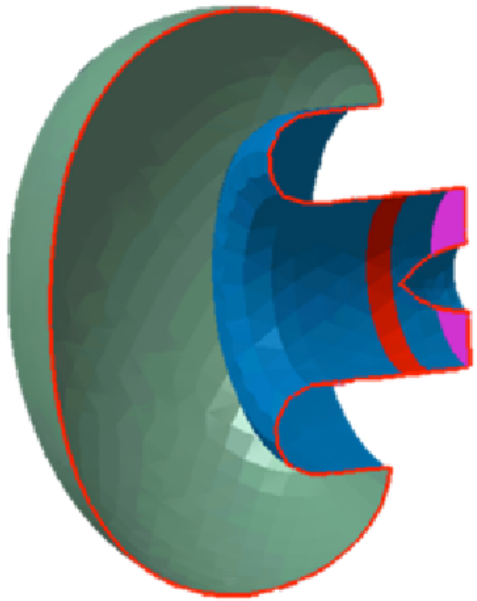

- Blue: hard-wall boundary.
- Red: impedance boundary (Myers)
- Green: Non-reflecting boundary (PML)
- Pink: boundary where the incoming duct mode is injected

FEM: applications in aeroacoustics

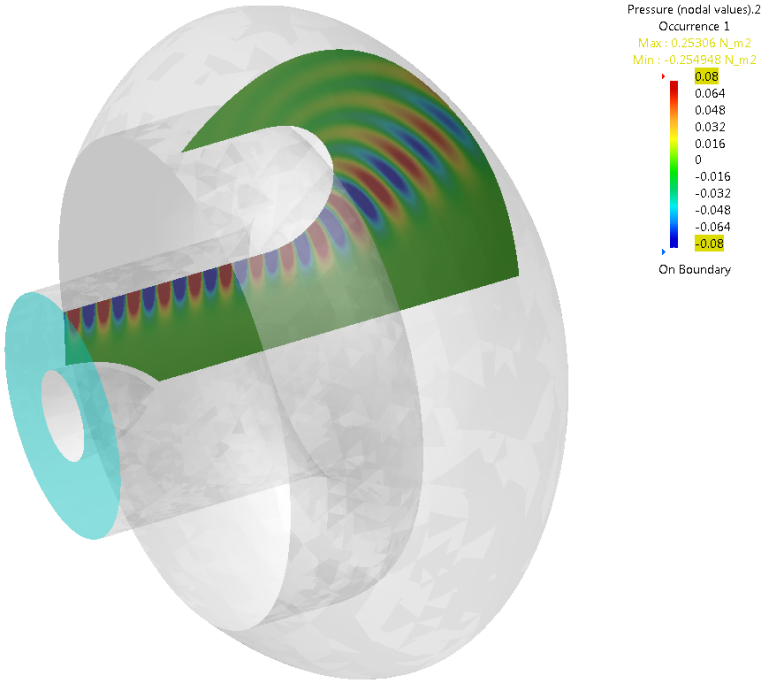

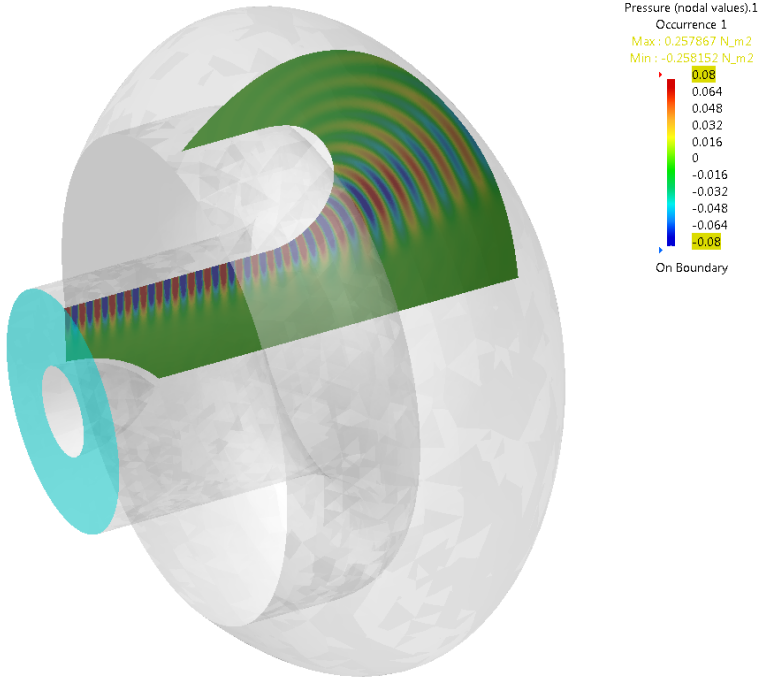

- Mode (13,0) at 9600rpm - 4480Hz
- From $p = 3$ to $p = 7$
- 3mn15s using MUMPS (10 threads)
- required **32.5 Gb of RAM**

- Mode (13,0) at 13500rpm - 6300Hz
- From $p = 4$ to $p = 10$
- 18mn10s using Mumps (10 threads)
- required **112.9 Gb of RAM**

Computed using high-order adaptive Simcenter Acoustic solver (Bériot and Gabard, 2019).

Comparison of prediction and measurements.

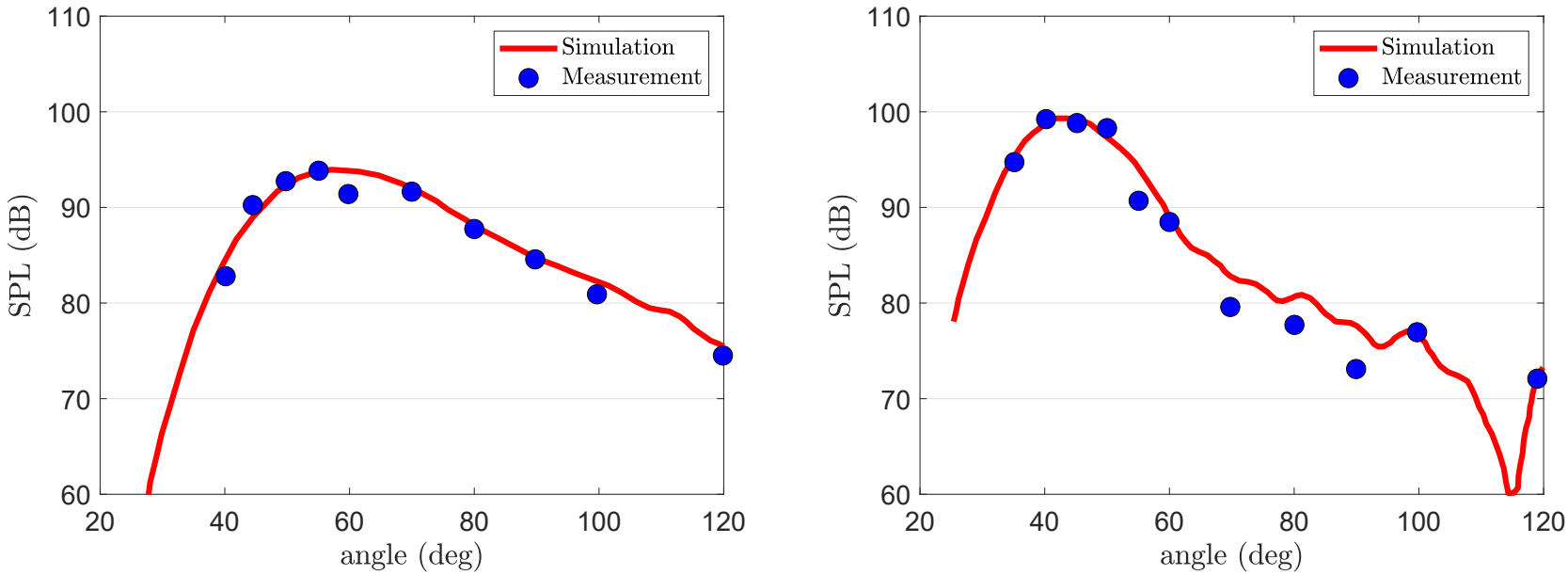

Without liner at 6750 rpm (left) and 9600 rpm (right)

- Good agreement with the experiments
- CAA tools can be used to limit costly physical testing

Example of results: effect of barrel liners.

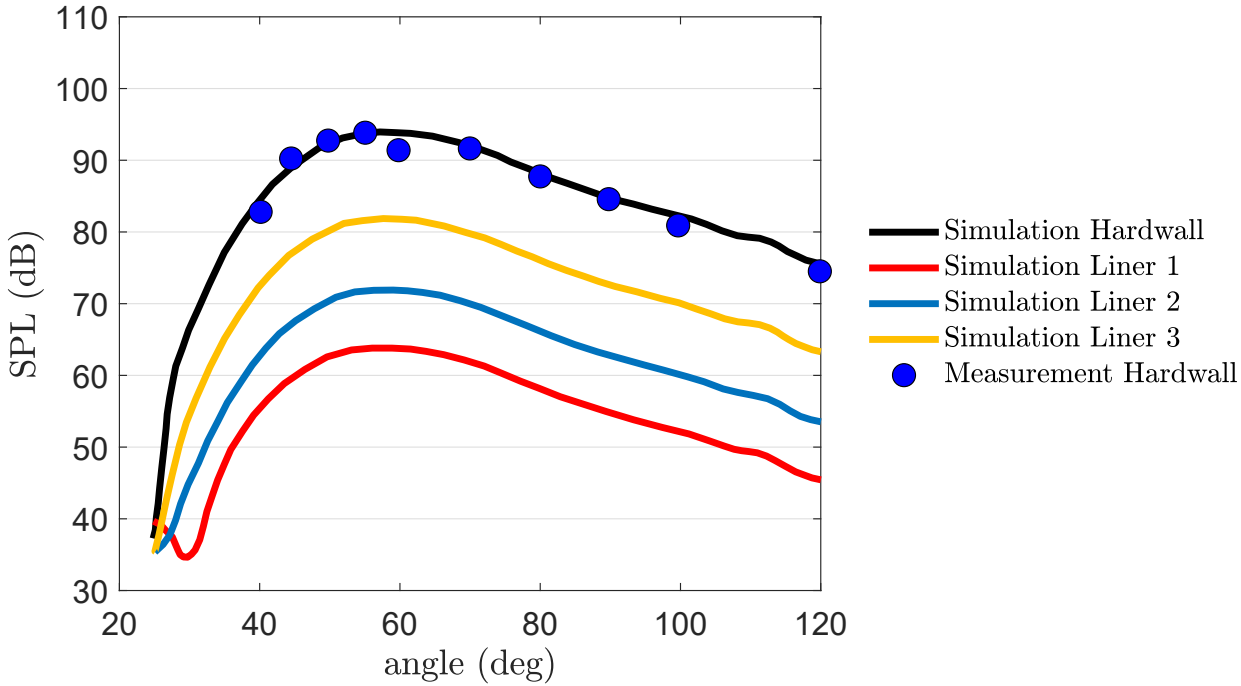

Prediction with several liners at 6750 rpm

FEM: applications in aeroacoustics

Upper frequency limit dictated by the memory resources

- For higher frequencies, Domain Decomposition (DDM) may be used
- Well established for Helmholtz problems (Farhat and Roux, 1991; Boubendir et al., 2012; Vion and Geuzaine, 2014)
- Only recently explored for flow acoustics (Lieu et al., 2020)

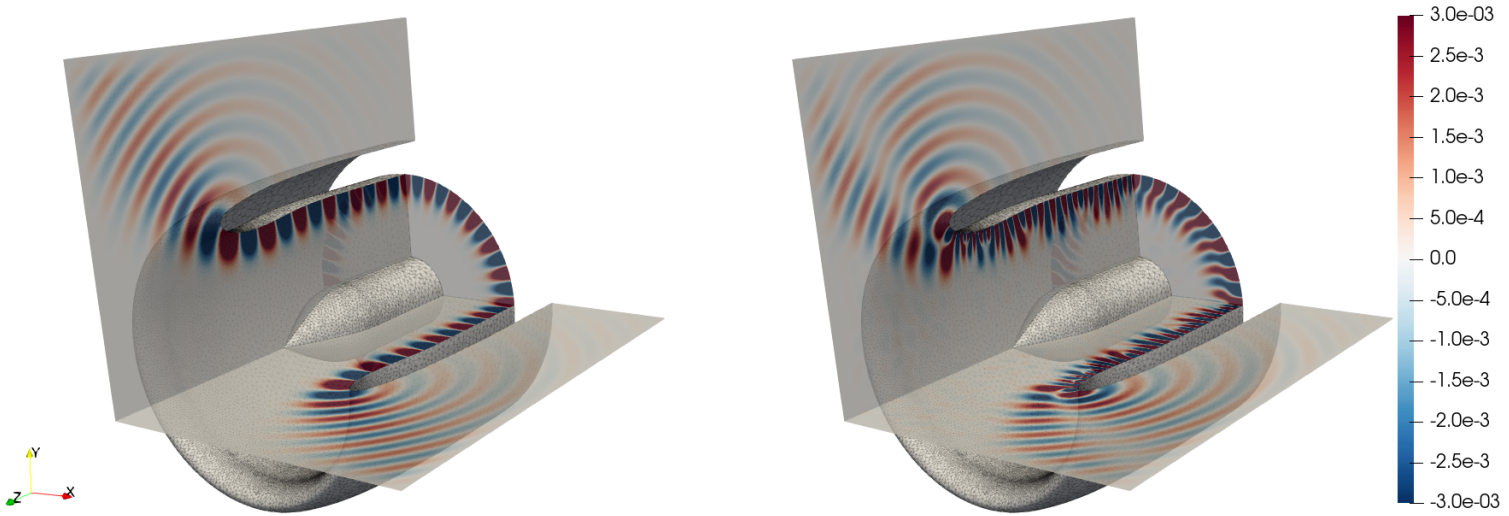

(c) Approach (d) Sideline

Figure: Real part of the acoustic potential obtained for the mode $(24, 1)$ at the first BPF ($f = 1300$ Hz) for two static flow configurations. The solutions were obtained with six sub-domains, from Lieu et al., 2020

FEM: applications in aeroacoustics

- Another significant source of aircraft noise is the sound generated at engine exhaust
- Main contributions are (Astley, 2009)
  - fan/core noise propagating through the rear arc
  - jet noise
- Complex refraction effects in non-isothermals flows require solving LEE
- Solving LEE in the frequency domain allows to avoid Kelvin-Helmholtz instability (Agarwal et al., 2004; Angeloski et al., 2014).
- Several frequency domain LEE solvers have then been proposed (Rao and Morris, 2006; Iob et al., 2010; Hamiche et al., 2019)

FEM: applications in aeroacoustics

Example: A realistic exhaust analysis in static-condition

- Developed during EU project TURNEX (Tester et al., 2008)
- Used to benchmark various CAA codes (Özyörük and Tester, 2010; Iob et al., 2010)
- Steady RANS computation, with hot core jet
- Hybrid LEE-LPE, solved with p-FEM adaptive model, from (Hamiche et al., 2019).

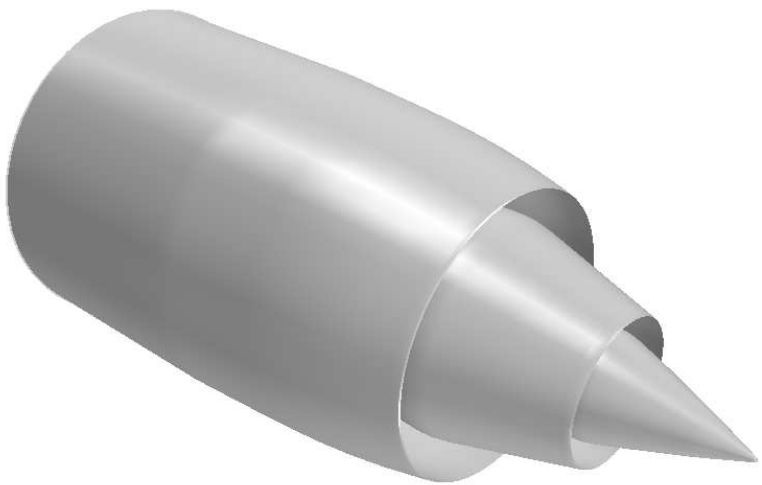

(a) TURNEX exhaust geometry

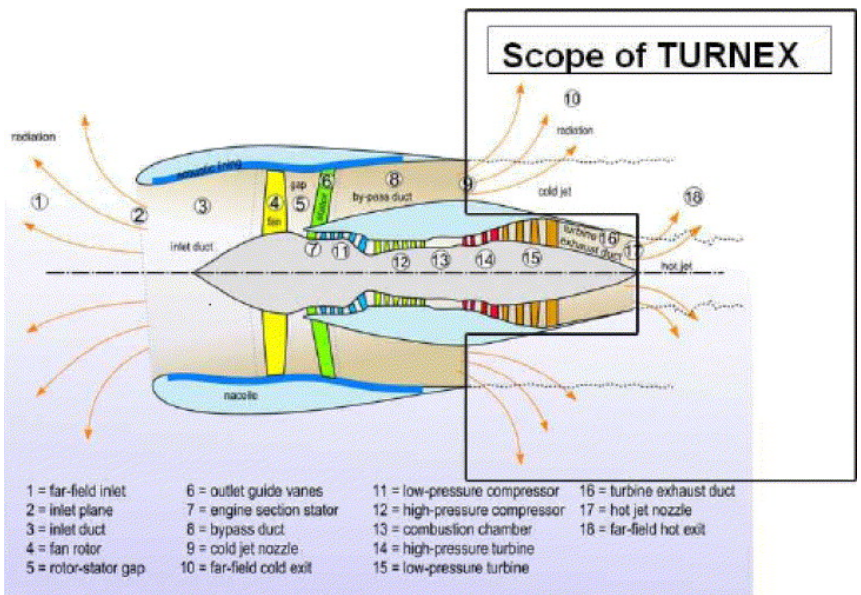

(b) Scope of TURNEX

FEM: applications in aeroacoustics

RANS mean flow first needs to be processed, with Boundary Layer Truncation (Hamiche et al., 2019)

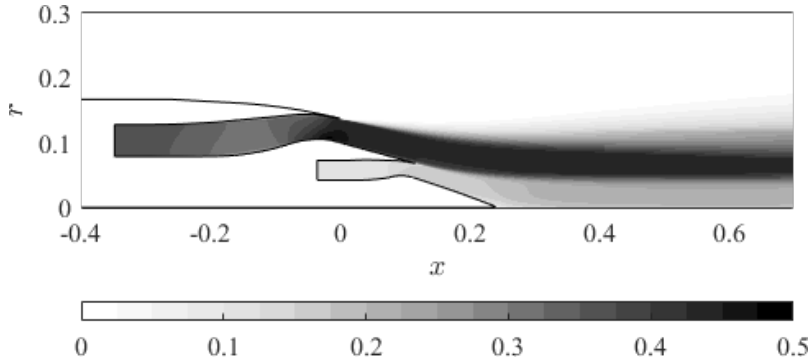

(c) Mach number M_0

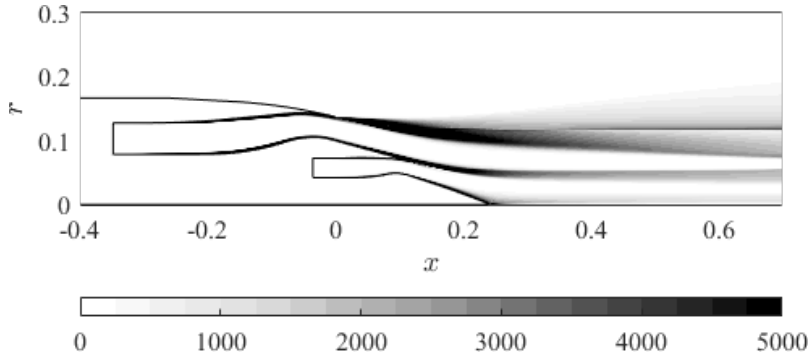

(d) Vorticity magnitude $|\omega_0| = |\nabla \times \boldsymbol{u}_0|$

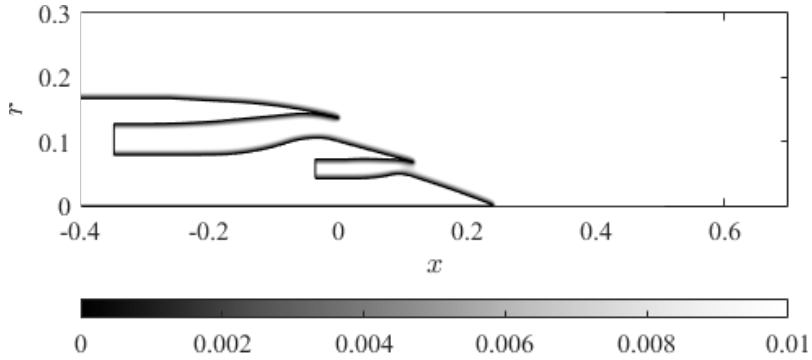

(e) Distance to wall d_{d}

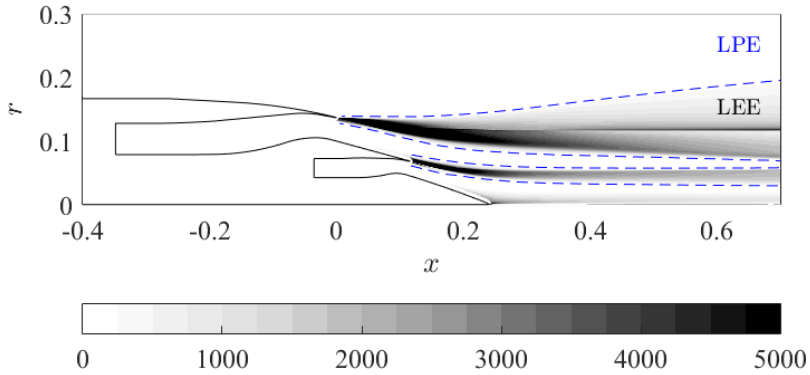

(f) Vorticity (after BLT) + LEE-LPE Coupling interface

FEM: applications in aeroacoustics

RANS mean flow then needs to be interpolated on acoustic mesh (mapping)

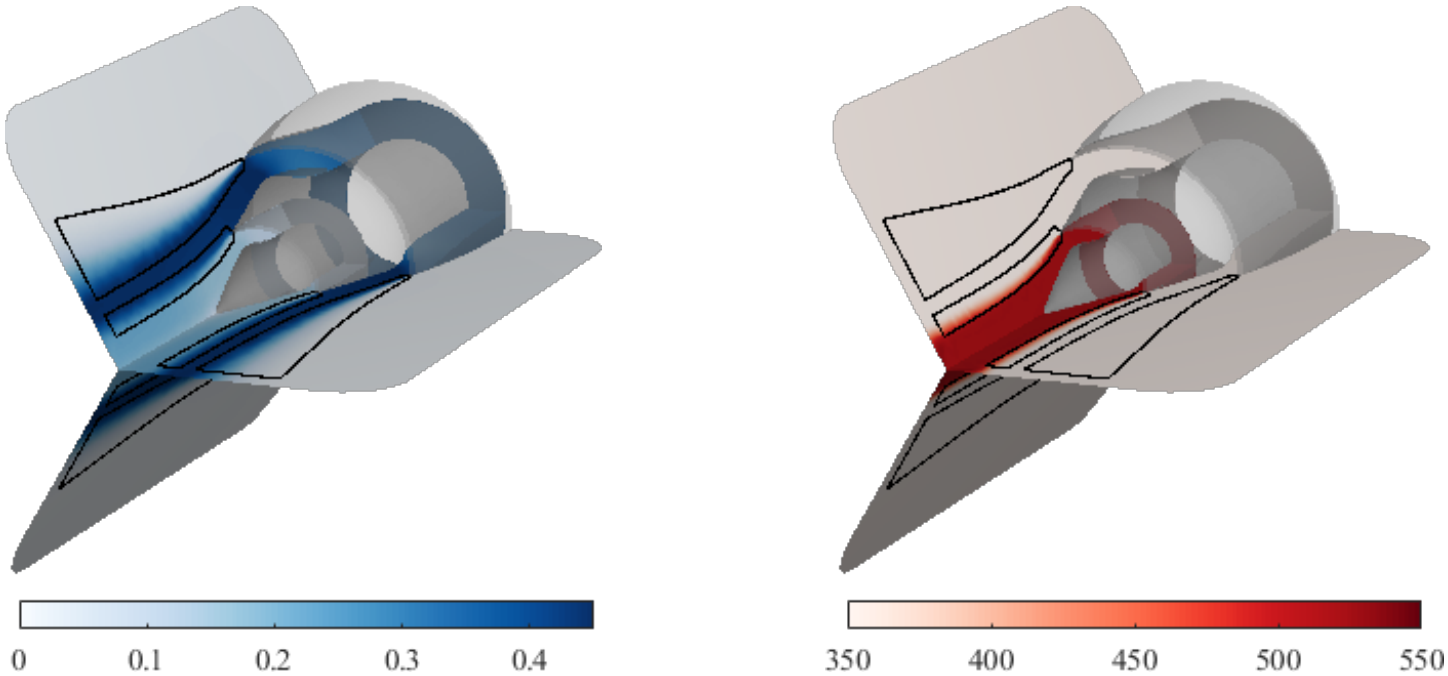

(g) Mach number M_0

(h) Speed of sound c_0, m/s

Figure: Interpolated mean flow for the short-cowl nozzle TURNEX test case under static approach condition. The LEE-LPE coupling interfaces in the bypass and core mixing regions are indicated by black solid lines, from Hamiche et al., 2019

FEM: applications in aeroacoustics

A priori error indicator determines the order before the calculation

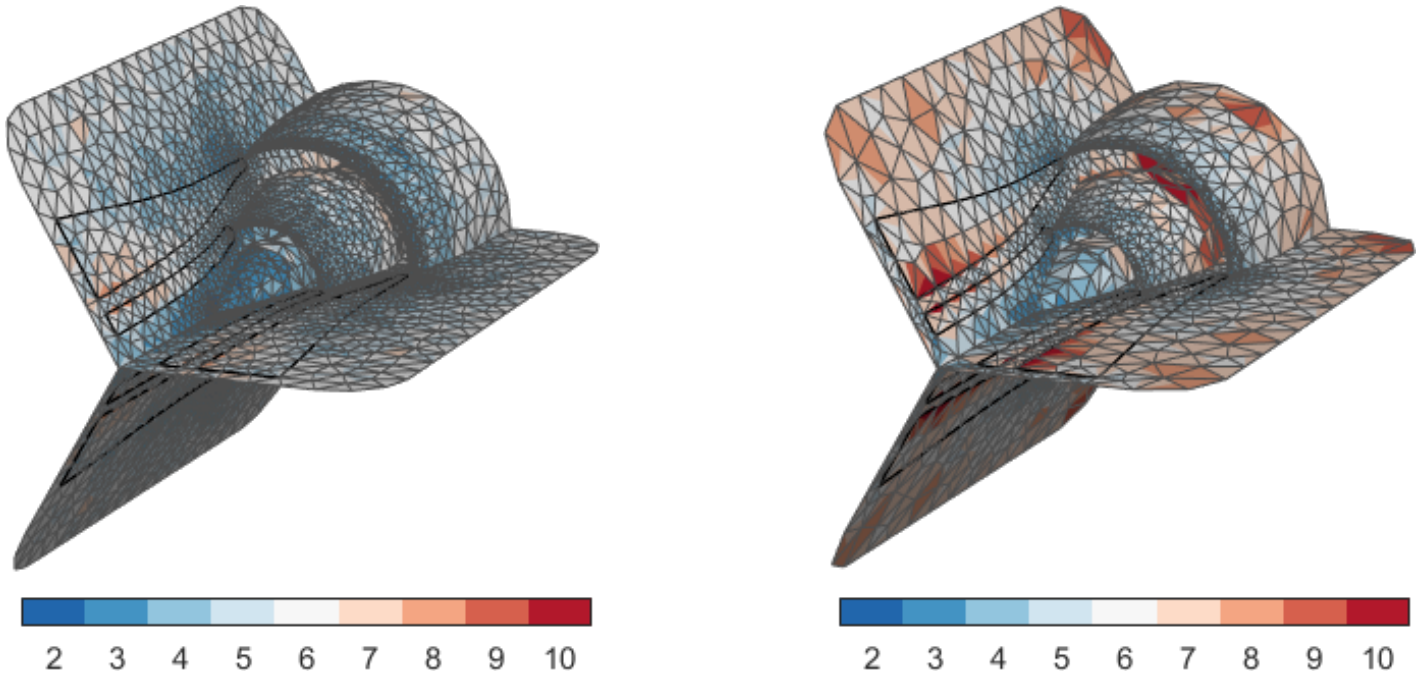

(a) Fine mesh $h = 4$ cm

(b) Coarse mesh $h = 6$ cm

Figure: Meshes and element order distribution for the short-cowl nozzle TURNEX test case under static approach condition at $f = 7497$ Hz (target accuracy $E_T = 1\%$). The LEE-LPE coupling interfaces in the bypass and core mixing regions are indicated with straight lines, from Hamiche et al., 2019.

FEM: applications in aeroacoustics

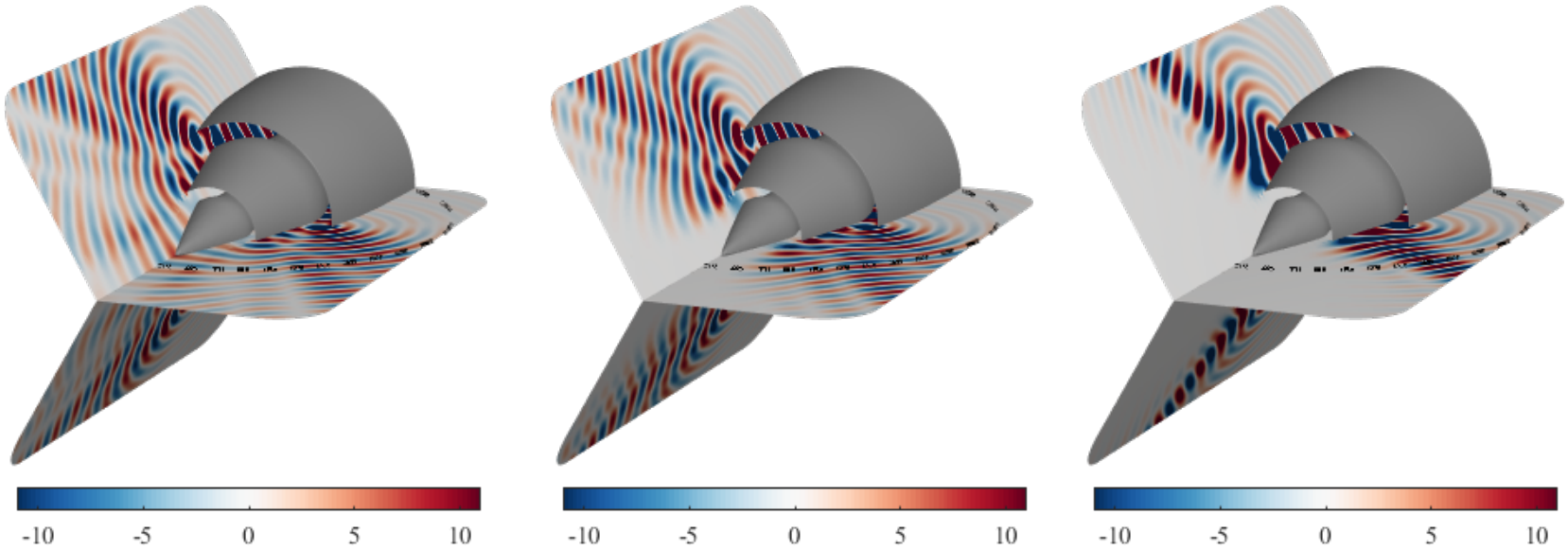

(a) Mode $(0, 1)$ (b) Mode $(4, 1)$ (c) Mode $(9, 1)$

Figure: Real part of pressure obtained with the adaptive hybrid LEE-LPE model, at 7497 Hz for various incident modes enforced in the bypass duct, from Hamiche et al., 2019

FEM: applications in aeroacoustics

Verification against a full LEE (axisymmetric) model.

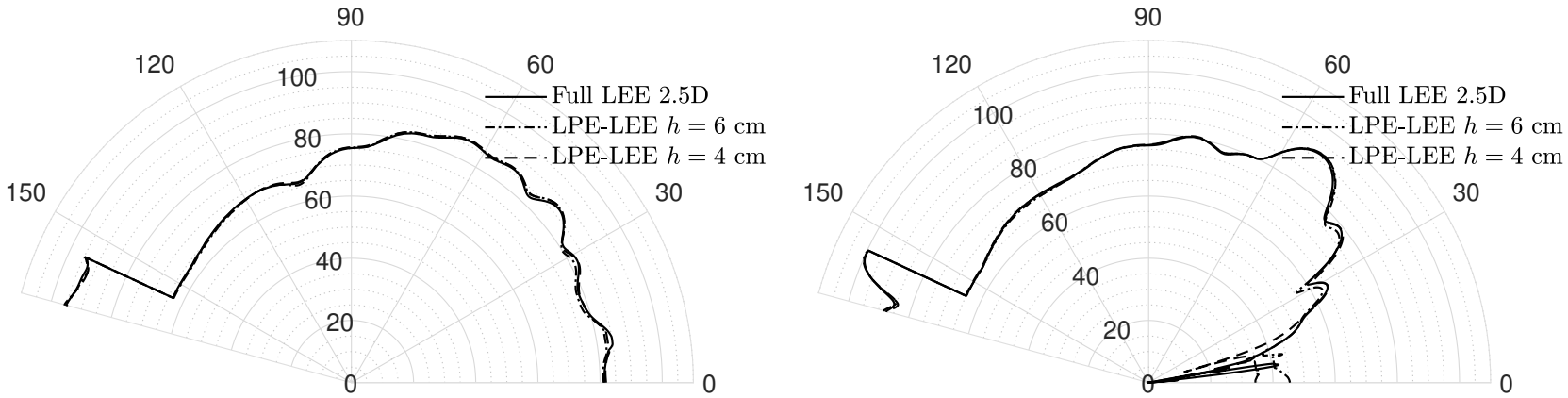

(a) Mode $(0, 1)$ (b) Mode $(9, 1)$

Figure: SPL directivities in dB along the control circle $\mathcal{C}$, for the short-cowl nozzle TURNEX exhaust radiation at $f = 7497$ Hz, from Hamiche et al., 2019.

Discontinuous Galerkin Methods

DGM: time-domain formulation

Start from a system of conservation equations:

$$\frac{\partial \mathbf{q}}{\partial t} + \frac{\partial \mathbf{f}_i(\mathbf{q})}{\partial x_i} = \mathbf{0} \, . \tag{13}$$

with $\mathbf{q}$ the vector of conserved quantities (mass, momentum, etc) and $\mathbf{f}_i$ the corresponding fluxes.

Apply a weighted residual approach and integrate by parts over each element Ω_m:

$$\int_{\Omega_m} \mathbf{w}^T \frac{\partial \mathbf{q}}{\partial t} - \frac{\partial \mathbf{w}^T}{\partial x_i} \mathbf{f}_i(\mathbf{q}) \, \mathrm{d}\Omega + \int_{\partial\Omega_m} \mathbf{w}^T \mathbf{f}_i(\mathbf{q}) n_i \, \mathrm{d}S = 0 \, , \tag{14}$$

where $\mathbf{w}$ is the test function and n_i is the normal to the element edges.

To ensure conservation, the flux should be continuous across the interface between two elements:

$$\mathbf{f}_i(\mathbf{q}_m) n_i = \mathbf{f}_i(\mathbf{q}_n) n_i = \tilde{\mathbf{f}}_{mn}(\mathbf{q}_m, \mathbf{q}_n) \, , \tag{15}$$

where $\tilde{\mathbf{f}}$ is the numerical flux...

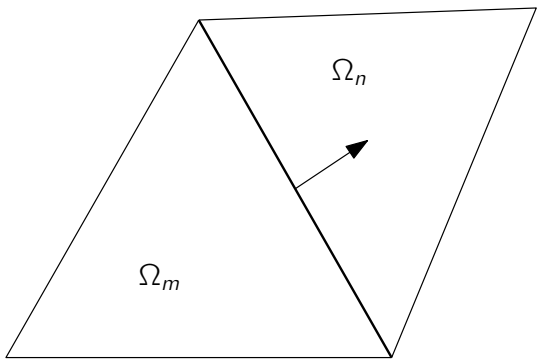

DGM: time-domain formulation

We now have the weak form:

$$\int_{\Omega_m} \mathbf{w}^T \frac{\partial \mathbf{q}}{\partial t} - \frac{\partial \mathbf{w}^T}{\partial x_i} \mathbf{f}_i(\mathbf{q}) \, \mathrm{d}\Omega + \int_{\partial\Omega_m} \mathbf{w}^T \mathbf{f}_{mn}(\mathbf{q}_m, \mathbf{q}_n) \, \mathrm{d}S = 0 \, . \tag{16}$$

By integrating by parts we can write the 'strong form':

$$\int_{\Omega_m} \mathbf{w}^T \left[\frac{\partial \mathbf{q}}{\partial t} + \frac{\partial \mathbf{f}_i(\mathbf{q})}{\partial x_i} \right] \mathrm{d}\Omega + \int_{\partial\Omega_m} \mathbf{w}^T \left[\mathbf{f}_{mn}(\mathbf{q}_m, \mathbf{q}_n) - \mathbf{f}_i(\mathbf{q}_m) n_i \right] \mathrm{d}S = 0 \, , \tag{17}$$

which is is less stringent for the test function $\mathbf{w}$ (it doesn't have to be smooth).

DGM: numerical flux

Question: How can we choose a unique definition of the flux $\mathbf{f}_{mn}$ across an interface between two elements when the solution is discontinuous across this interface?

- If we can calculate the evolution of an initial condition that is piecewise constant and with a single discontinuity (Riemann problem),
- then we can define the corresponding flux at the interface.

There is a LARGE number of numerical fluxes available in the literature. See textbooks on the subject (Toro, 1999; Leveque, 2002; Hirsch, 2007).

Example: the characteristics-based numerical flux for a linear problem $\mathbf{f}(\mathbf{q}) = \mathbf{F}\mathbf{q}$:

$$\mathbf{f}_{mn}(\mathbf{q}_m, \mathbf{q}_n) = \frac{1}{2}\left[\mathbf{F}\mathbf{q}_m + \mathbf{F}\mathbf{q}_n - \theta|\mathbf{F}|(\mathbf{q}_m - \mathbf{q}_n)\right] , \tag{18}$$

with $|\mathbf{F}| = \mathbf{W}|\mathbf{\Lambda}|\mathbf{W}^{-1}$ with $\mathbf{\Lambda}$ and $\mathbf{W}$ the eigenvalues and eigenvectors of $\mathbf{F}$.

- Centred scheme $\theta = 0$ (averaging the fluxes on either sides of the discontinuity).
- Fully upwind scheme $\theta = 1$, corresponding to the exact characteristics-based flux (exact Roe solver).

DGM: spatial discretization

Modal description: the solution $\mathbf{q}$ is written as a sum of variable order polynomials $P_n(\mathbf{x})$ defined on a reference element:

$$\mathbf{q}(\mathbf{x}, t) = \sum_n \mathbf{q}_n(t) P_n(\mathbf{x}) \, . \qquad (19)$$

- Ideally orthogonal to improve conditioning.
- Typically based on Jacobi polynomials (including Legendre polynomials).
- Nodal shape functions ψ_n are related to polynomials $P_n(\mathbf{x})$ through a Vandermond matrix.
- See textbook by Hesthaven and Warburton (2007).

Example of orthonormal polynomials of order (i, j) on the equilateral.

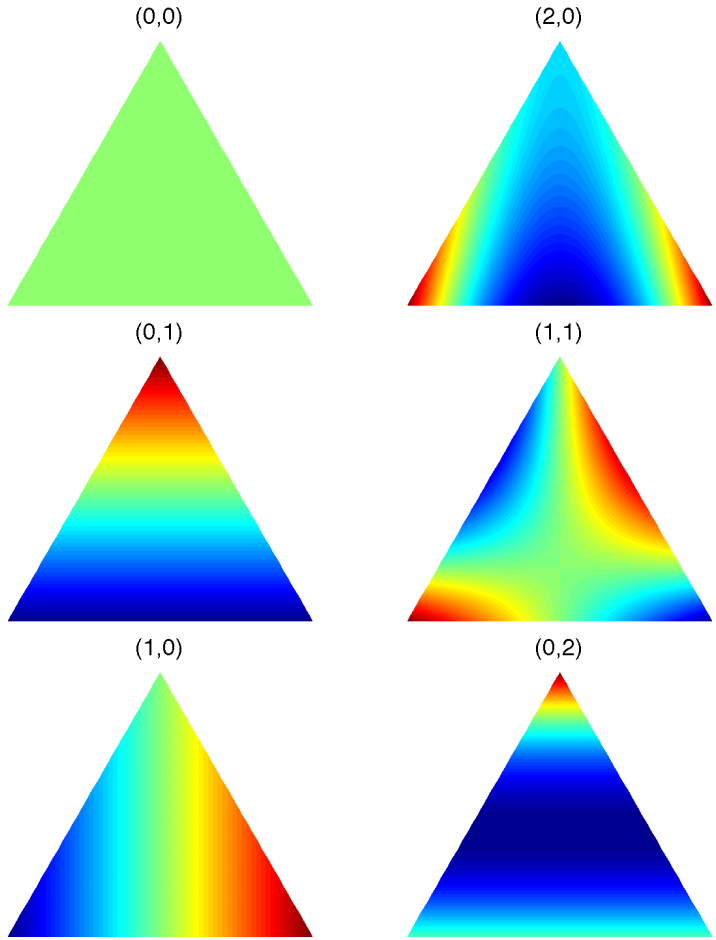

DGM: spatial discretization

Nodal interpolation: the solution $\mathbf{q}$ is defined at several nodes $\mathbf{x}_n$ on each element and the high-order interpolation is constructed from these nodal values.

$$\mathbf{q}(\mathbf{x}, t) = \sum_n \mathbf{q}(\mathbf{x}_n, t)\psi_n(\mathbf{x}) \ . \qquad (20)$$

- ψ_n are nodal shape functions.
- Nodes can be optimised to improve the stability of the discrete model.
- Nodes on edges between elements are duplicated.
- Defined for 1D, 2D (triangle, quadrangle) and 3D elements.

Examples of α-optimized node positions on the triangle, calculated from Hesthaven and Warburton (2007).

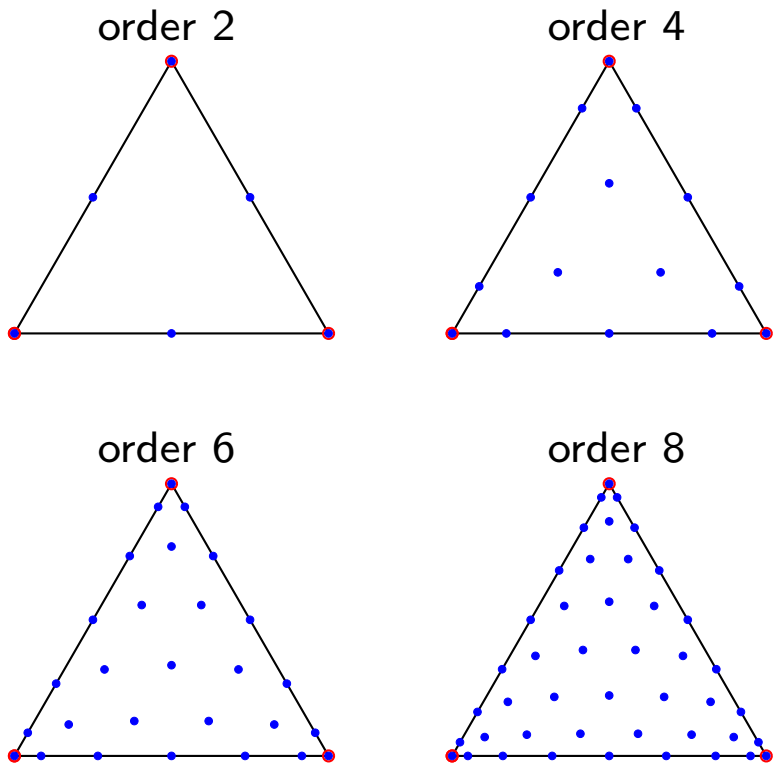

DGM: spatial discretization

Modal vs nodal:

- Degrees of freedom in the discrete model can be modal $\mathbf{q}_n(t)$ or nodal $\mathbf{q}(\mathbf{x}_n, t)$.
- Nodal description is particularly convenient for the calculation of fluxes (only involve local calculations).
- It is important to choose the node positions so as to improve the conditioning of the Vandermond matrix, otherwise high-order interpolations might be unstable.
- For non-linear problems the two descriptions can be used in different ways, but they are not equivalent in terms of efficiency, accuracy and stability, see section 5.2 in Hesthaven and Warburton (2007).

DGM: discrete form

After discretising we obtain a system of coupled ODEs for each element:

$$\mathbf{M}_m \frac{\partial \mathbf{Q}_m}{\partial t} = \mathbf{D}_m \mathbf{F}(\mathbf{Q}_m) + \sum_{n \in \mathcal{N}_m} \mathbf{L}_{mn} \mathbf{F}(\mathbf{Q}_m, \mathbf{Q}_n) \,, \tag{21}$$

with $\mathbf{M}_m$ the mass matrix, $\mathbf{D}_m$ the divergence matrix, $\mathbf{L}_m$ the 'lifting matrix' (contribution from the fluxes on the element boundaries). $\mathcal{N}_m$ is the set of neighbours of element m.

Time integration:

- Explicit formulation, a key benefit of DGM.
- The choice of time step and the definition of the CFL number depend on the order of interpolation p.

$$\Delta t \leq C \frac{\Delta x}{p|a|} \,, \tag{22}$$

- Common choices are optimized Runge–Kutta schemes, for instance Hu et al. (1996) and Bogey and Bailly (2004).
- Comparison of different schemes by Toulorge (2012).

DGM: quadrature-free implementation

Atkins and Shu (1998) realised that for elements with constant Jacobians (triangles in 2D and tetrahedra in 3D) the calculation of the element matrices $\mathbf{M}_m$, $\mathbf{D}_m$ and $\mathbf{L}_m$ can be simplified. For instance for the mass matrix:

$$(\mathbf{M}_m)_{ij} = \int_{\Omega_m} P_i P_j \, \mathrm{d}x\mathrm{d}y \tag{23}$$

$$= J_m \int_{\Omega_{\mathrm{ref}}} P_i P_j \, \mathrm{d}u\mathrm{d}v = J_m \left(\mathbf{M}_{\mathrm{ref}}\right)_{ij} \ . \tag{24}$$

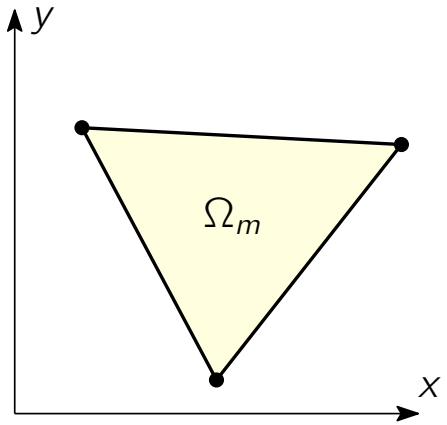

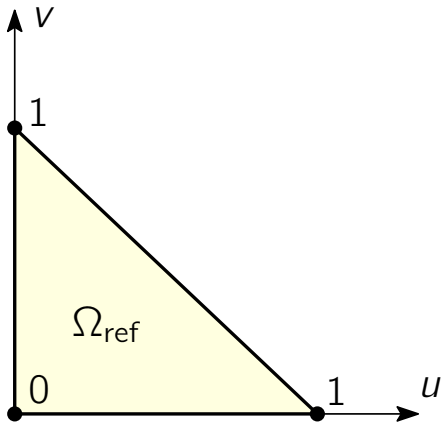

- No need to calculate and store element matrices for every elements.
- Large reduction in memory requirements. Significant impact on performance (cache efficiency and memory bandwidth).
- But significant constraint on the geometry description...

DGM: properties

Interpolation error: Similar behaviour to FEM.

Dispersion properties: depend on the governing equations, the DG formulation and the choice of numerical flux. For standard DGM for the advection equation Hu and Atkins (2002) and Ainsworth (2004b) have obtained the following results:

- The relative dispersion error scales like $(kh)^{2p+2}$.
- The dissipation rate $\mathrm{Im}(\tilde{\omega})/\omega$ scales like $(kh)^{2p+1}$.

Some instance of superconvergence have been reported for specific governing equations and choice of numerical flux.

Warning: This is valid for smooth solutions. Problems involving singular or discontinuous solutions require special treatments (flux limiting, artificial viscosity...), typically for shock capturing methods (Persson and Peraire, 2006; Sheshadri and Jameson, 2014).

DGM: application to aeroacoustics

- First use of a DG method for aeroacoustics (Atkins, 1997; Atkins and Shu, 1998).
- Initially efforts concentrated on solving the Linearised Euler Equations. The Acoustic Perturbation Equations have also been considered. More recently solving the full compressible Navier-Stokes equations for DNS calculations.
- The DGM is well suited for
  - Exhaust noise propagation due to the refraction effect through the jet shear layer.
  - Large 3D problems (good scaling of computational cost with problem size).
- Also used for frequency-domain calculations (Rao, 2004; Lario et al., 2013), but less efficient than FEM.

DGM: application to aeroacoustics

Direct numerical simulations of 3D flows around an aerofoil, including the generation and propagation of trailing edge noise (Flad et al., 2014).

Flow structures (Q criterion)

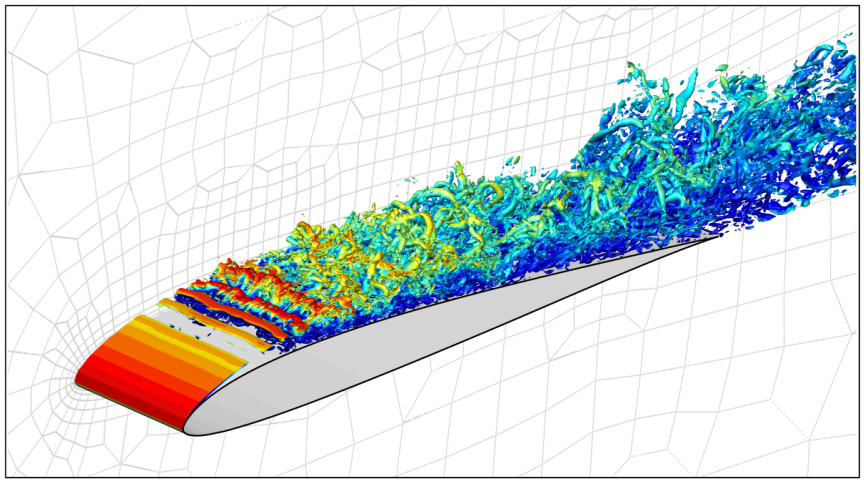

Sound field
(rate of dilatation)

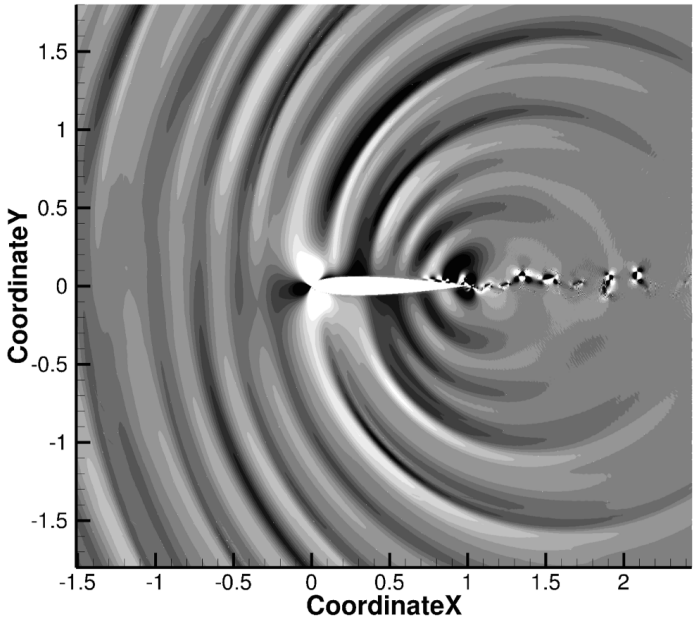

DGM: application to aeroacoustics

Noise radiation from a 3D ‘drooped’ intake including the mean flow angle of incidence and the mean flow distortion (Rarata, 2014).

mean flow (steady Euler)

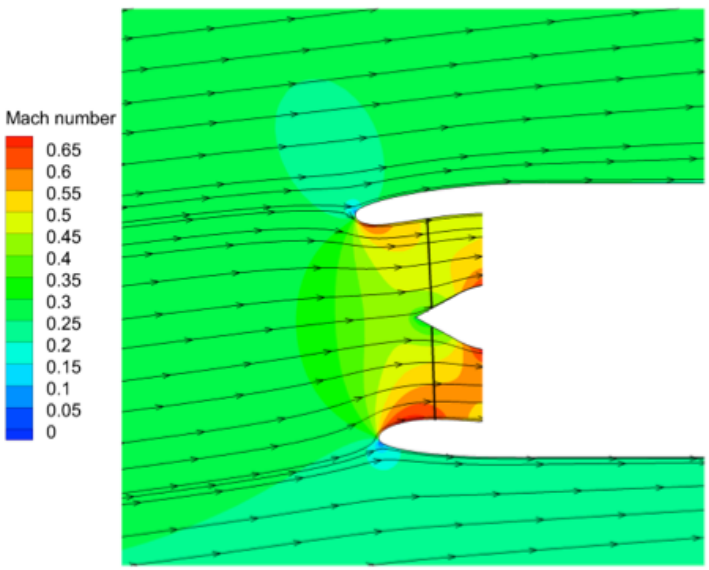

acoustic streamlines

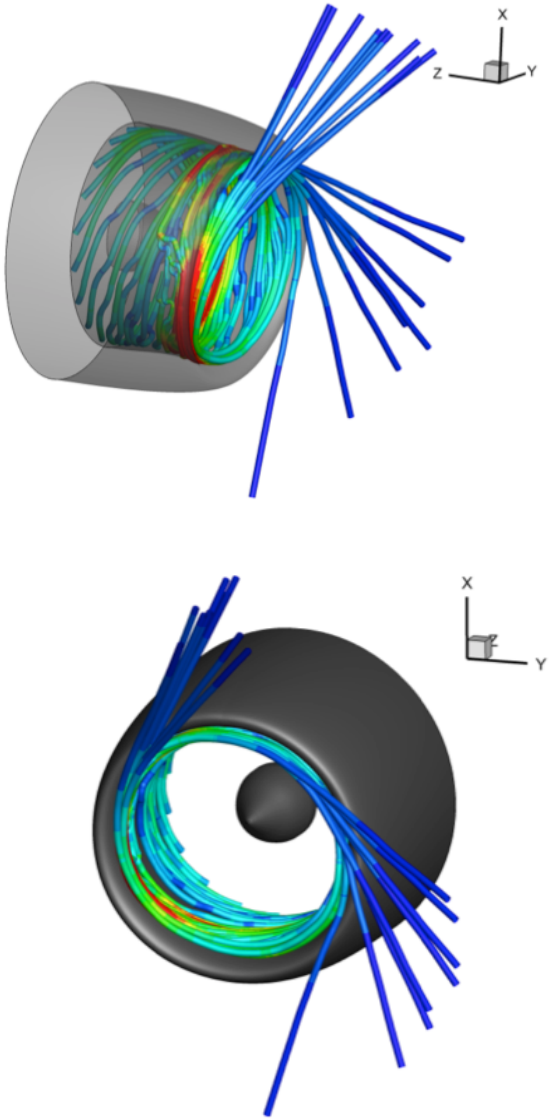

DGM: application to aeroacoustics

The TURNEX geometry was modified to include chevrons (Williamschen et al., 2016)

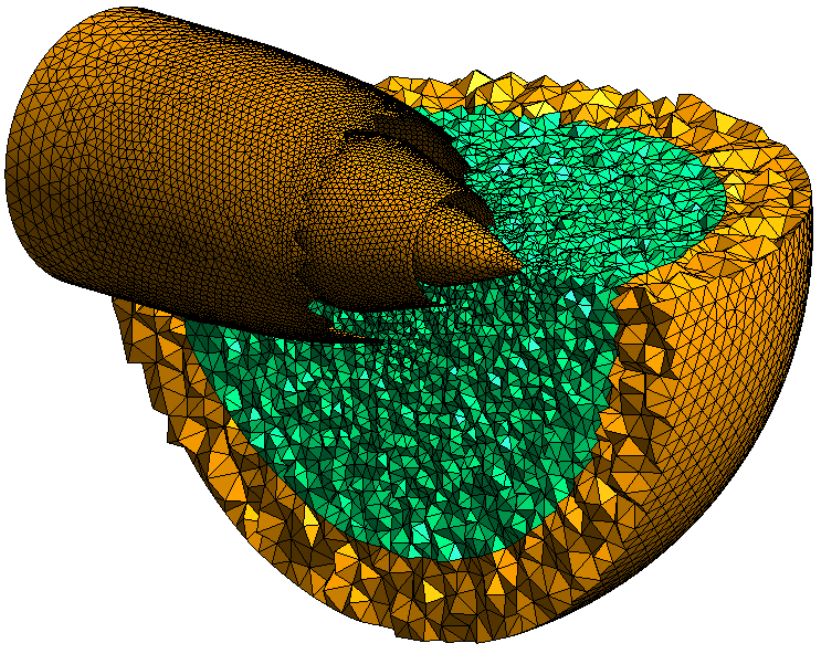

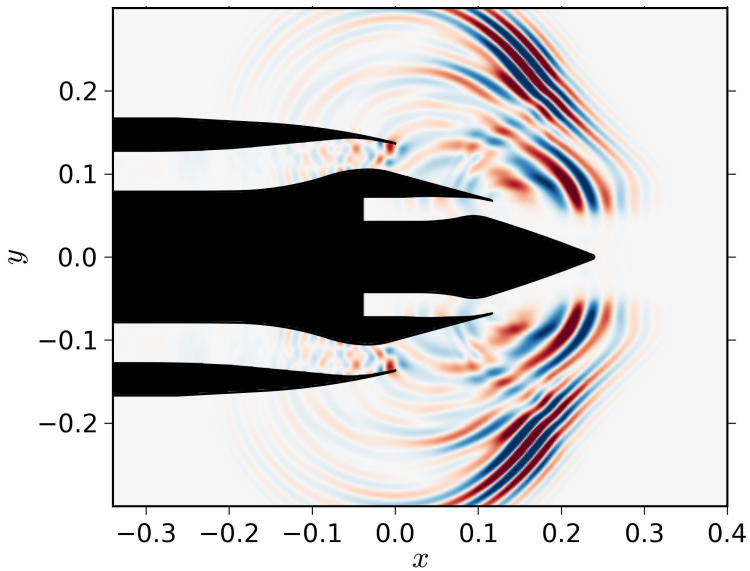

Figure: Section of the aeroacoustic mesh for the modified TURNEX geometry (left) , instantaneous contours of p'_c on a $x-y$ slice of the computational domain at time $t = 0.002$ s for the acoustic mode $(10, 0)$, with color scale from -10^{-4} to 10^{-4} (right), from (Williamschen et al., 2016).

Conclusions

- Overview of methods used for propagating sound in non-uniform flows
- Two methods presented in detail
  - FEM for linearized potential theory in frequency domain
  - DGM for LEE in time domain
- Frequency domain methods are robust, especially when combined with adaptive p-FEM, but they heavily rely on efficient solvers for large sparse problems
- Time domain methods scale well with problem size but they suffer from linear instabilities
- Interaction between the sound field and the liner in the presence of a boundary layer poses some theoretical issues
- Another challenge is the integration with other tools (source description, CFD mapping)

References I

Abrahamson, A. (1977). "A finite element algorithm for sound propagation in axisymmetric ducts containing compressible mean flow". In: *AIAA 4th Aeroacoustics Conference*. AIAA Paper 1977-1301.

Agarwal, A., P. Morris and R. Mani (2004). "Calculation of sound propagation in nonuniform flows: suppression of instability waves". In: *AIAA Journal* 42.1, pp. 80–88.

Ainsworth, M. (2004a). "Discrete dispersion relation for *hp*-version finite element approximation at high wave number". In: *SIAM Journal on Numerical Analysis* 42.2, pp. 553–575.

— (2004b). "Dispersive and dissipative behaviour of high order discontinuous Galerkin finite element methods". In: *Journal of Computational Physics* 198.1, pp. 106–130.

Angeloski, A. et al. (2014). "Challenges for time and frequency domain aeroacoustic solvers". In: *11th World Congress on Computational Mechanics (WCCM XI)*. Barcelona.

Astley, R. J. and W. Eversman (1981). "Acoustic transmission in non-uniform ducts with mean flow, Part II: the finite element method". In: *Journal of Sound and Vibration* 74.1, pp. 103–121.

— (1988). "Wave envelope elements for acoustical radiation in inhomogeneous media". In: *Computers & Structures* 30.4, pp. 801–810.

Astley, R. (1985). "A finite element, wave envelope formulation for acoustical radiation in moving flows". In: *Journal of Sound and Vibration* 103.4, pp. 471–485.

Astley, R. (2000). "Infinite elements for wave problems: a review of current formulations and an assessment of accuracy". In: *International Journal for Numerical Methods in Engineering* 49, pp. 951–976.

References II

Astley, R. (2009). "Numerical methods for noise propagation in moving flows, with application to turbofan engines". In: *Acoustical Science and Technology* 30.4, pp. 227–239.

Astley, R. et al. (2002). "Modelling tone propagation from turbofan inlets". In: AIAA paper 2002-2449.

Atkins, H. (1997). "Continued development of the discontinuous Galerkin method for computational aeroacoustic applications". In: *AIAA Paper*.

Atkins, H. L. and C.-W. Shu (1998). "Quadrature-free implementation of discontinuous Galerkin method for hyperbolic equations". In: *AIAA Journal* 36.5, pp. 775–782.

Bécache, E., S. Fauqueux and P. Joly (2003). "Stability of perfectly matched layers, group velocities and anisotropic waves". In: *Journal of Computational Physics* 188, pp. 399–433.

Bayliss, A., C. I. Goldstein and E. Turkel (1985). "On accuracy conditions for the numerical computation of waves". In: *Journal of Computational Physics* 59.3, pp. 396–404.

Bériot, H and A Modave (2020). "An automatic PML for acoustic finite element simulations in convex domains of general shape". In: *International Journal for Numerical Methods in Engineering*.

Bériot, H. and G. Gabard (2019). "Anisotropic adaptivity of the p-FEM for time-harmonic acoustic wave propagation". In: *Journal of Computational Physics* 378, pp. 234–256.

Bériot, H., G. Gabard and E. Perrey-Debain (2013). "Analysis of high-order finite elements for convected wave propagation". In: *International Journal for Numerical Methods in Engineering* 96.11, pp. 665–688.

References III

Bériot, H., A. Prinn and G. Gabard (2016). "Efficient implementation of high-order finite elements for Helmholtz problems". In: *International Journal for Numerical Methods in Engineering* 106.3, pp. 213–240.

Bogey, C. and C. Bailly (2004). "A family of low dispersive and low dissipative explicit schemes for flow and noise computations". In: *Journal of Computational Physics* 194, pp. 194–214.

Boubendir, Y., X. Antoine and C. Geuzaine (2012). "A quasi-optimal non-overlapping domain decomposition algorithm for the Helmholtz equation". In: *Journal of Computational Physics* 231.2, pp. 262–280.

Engquist, B. and A. Majda (1977). "Absorbing boundary conditions for the numerical simulation of waves". In: *Mathematics of Computation* 31, pp. 629–651.

Ernst, O. G. and M. J. Gander (2012). "Why it is difficult to solve Helmholtz problems with classical iterative methods". In: *Numerical analysis of multiscale problems*. Springer, pp. 325–363.

Eversman, W. (1991). *Theoretical models for duct acoustics*. Reference publication. NASA.

— (2001). "The boundary condition at an impedance wall in a non-uniform duct with potential mean flow". In: *Journal of Sound and Vibration* 246.1, pp. 63–69.

Eversman, W. and R. J. Astley (1981). "Acoustic transmission in non-uniform ducts with mean flow, Part I: The method of weighted residuals". In: *Journal of Sound and Vibration* 74.1, pp. 89–101.

Farhat, C. and F.-X. Roux (1991). "A method of finite element tearing and interconnecting and its parallel solution algorithm". In: *International Journal for Numerical Methods in Engineering* 32.6, pp. 1205–1227.

References IV

Flad, D. G. et al. (2014). "A Discontinuous Galerkin Spectral Element Method for the Direct Numerical Simulation of Aeroacoustics". In: *20th AIAA/CEAS Aeroacoustics Conference*. AIAA paper 2014-2740.

Frey, P. and P.-L. George (2010). *Mesh generation*. Vol. 32. John Wiley & Sons.

Gabard, G et al. (2018). "Adaptive, high-order finite-element method for convected acoustics". In: *AIAA Journal* 56.8, pp. 3179–3191.

Goldstein, M. (1976). *Aeroacoustics*. New York, McGraw-Hill International Book Co.

— (2001). "An exact form of Lilley's equation with a velocity quadrupole/temperature dipole source term". In: *Journal of Fluid Mechanics* 443, pp. 231–236.

Hamiche, K. et al. (2019). "Hybrid numerical model for acoustic propagation through sheared flows". In: *Journal of Sound and Vibration* 463, p. 114951.

Hamilton, J. A. and R. J. Astley (2005). "Acoustic propagation on irrotational mean flows using transient finite and infinite elements". In: *AIAA journal* 43.1, pp. 124–134.

Hesthaven, J. S. and T. Warburton (2007). *Nodal discontinuous Galerkin methods: algorithms, analysis, and applications*. Springer.

Hirsch, C. (2007). *Numerical Computation of Internal and External Flows: The Fundamentals of Computational Fluid Dynamics: The Fundamentals of Computational Fluid Dynamics*. Vol. 1. Butterworth-Heinemann.

Horowitz, S., R. Sigman and B. Zinn (1986). "An iterative finite element-integral technique for predicting sound radiation from turbofan inlets in steady flight". In: *AIAA Journal* 24.8, pp. 1256–1262.

References V

Hu, F., M. Y. Hussaini and J. Manthey (1996). "Low-dissipation and low-dispersion Runge–Kutta schemes for computational acoustics". In: *Journal of Computational Physics* 124.1, pp. 177–191.

Hu, F. Q. (2008). "Development of PML absorbing boundary conditions for computational aeroacoustics: A progress review". In: *Computers & Fluids* 37.4, pp. 336–348.

Hu, F. Q. and H. L. Atkins (2002). "Eigensolution analysis of the discontinuous Galerkin method with nonuniform grids: I. one space dimension". In: *Journal of Computational Physics* 182.2, pp. 516–545.

Hughes, T. J., J. A. Cottrell and Y. Bazilevs (2005). "Isogeometric analysis: CAD, finite elements, NURBS, exact geometry and mesh refinement". In: *Computer methods in applied mechanics and engineering* 194.39, pp. 4135–4195.

Ihlenburg, F. and I. Babuška (1997). "Finite element solution to the Helmholtz equation with high wave number – Part II: the *h*-*p*-version of the FEM". In: *SIAM Journal of Numerical Analysis* 34.1, pp. 315–358.

Ihlenburg, F. (1998). *Finite element analysis of acoustic scattering*. Vol. 132. Springer.

Ihlenburg, F. and I. Babuška (1995). "Dispersion analysis and error estimation of Galerkin finite element methods for the Helmholtz equation". In: *International Journal for Numerical Methods in Engineering* 38.22, pp. 3745–3774.

Iob, A., R. Arina and C. Schipani (2010). "Frequency-Domain linearized Euler model for turbomachinery noise radiation through engine exhaust". In: *AIAA Journal* 48.4, pp. 848–858.

References VI

Lan, J. H., Y. Guo and C. Breard (2004). "Validation of acoustic propagation code with JT15D static and flight test data". In: *10th AIAA/CEAS Aeroacoustics Conference*. AIAA Paper 2004-2986.

Lario, A., R. Arina and A. Iob (2013). "A Discontinuous Galerkin Method for the Solution of the Linearized Navier-Stokes Equations". In: *19th AIAA/CEAS Aeroacoustics Conference*. AIAA Paper 2013-2168.

Leveque, R. (2002). *Finite volume methods for hyperbolic problems*. Cambridge University Press.

Lieu, A. et al. (2020). "A non-overlapping Schwarz domain decomposition method with high-order finite elements for flow acoustics". In: *Computer Methods in Applied Mechanics and Engineering* 369, p. 113223.

Marchner, P et al. (2020). "Stable Perfectly Matched Layers with Lorentz transformation for the convected Helmholtz equation". In: *Under review in the Journal of Computational Physics*.

Modave, A., J. Lambrechts and C. Geuzaine (2017). "Perfectly matched layers for convex truncated domains with discontinuous Galerkin time domain simulations". In: *Computers & Mathematics with Applications* 73.4, pp. 684–700.

Mustafi, P. (2013). "Improved turbofan intake liner design and optimization". PhD thesis. University of Southampton.

Myers, M. (1980). "On the acoustic boundary condition in the presence of flow". In: *Journal of Sound and Vibration* 71.3, pp. 429–434.

References VII

Özyörük, Y. and B. Tester (2010). "Assessment of a frequency-domain linearised Euler solver for turbofan aft radiation predictions and comparison with measurements". In: *Procedia Engineering* 6, pp. 153–162.

Persson, P.-O. and J. Peraire (Jan. 2006). "Sub-Cell Shock Capturing for Discontinuous Galerkin Methods". In: *44th AIAA Aerospace Sciences Meeting and Exhibit*. Aerospace Sciences Meetings. AIAA Paper 2006-112. American Institute of Aeronautics and Astronautics.

Rao, P. (2004). "High order unstructured grid methods for computational aeroacoustics". Ph.D. Thesis. Pennsylvania State University.

Rao, P. and P. Morris (2006). "Use of finite element methods in frequency domain aeroacoustics". In: *AIAA Journal* 44.7, pp. 1643–1652.

Rarata, Z. (2014). "Application and assessment of time-domain DGM for solving 3D linearized Euler equations". PhD thesis. University of Southampton.

Sang, W. and Y. Shi (2013). "Comparison of Octree and Omni-Tree Cartesian Grid for Civil-Plane High-Lift Model Simulations". In: *Journal of Aircraft* 50.4, pp. 1099–1105.

Sheshadri, A. and A. Jameson (June 2014). "Shock detection and capturing methods for high order Discontinuous-Galerkin Finite Element Methods". In: *32nd AIAA Applied Aerodynamics Conference*. AIAA Aviation. AIAA Paper 2014-2688. American Institute of Aeronautics and Astronautics.

Sigman, R., R. Majjigi and B. Zinn (1978). "Determination of turbofan inlet acoustics using finite elements". In: *AIAA Journal* 16.11, pp. 1139–1145.

Šolín, P., K. Segeth and I. Doležel (2003). *Higher-order finite element methods*. New York: Chapman & Hall.

References VIII

Spieser, E. (2020). "Adjoint-based jet noise propagation model for the acoustic potential". PhD thesis. Ecole Centrale de Lyon.

Tester, B. J. et al. (2008). *TURNEX: Turbomachinery Noise Radiation through the Engine Exhaust. Publishable Final Activity Report*. Tech. rep. EU Project 516079.

Thompson, L. L. (2006). "A review of finite-element methods for time-harmonic acoustics". In: *Journal of the Acoustical Society of America* 119.3, pp. 1315–1330.

Toro, E. (1999). *Riemann solvers and numerical methods for fluid dynamics: a practical introduction*. Springer.

Toulorge, T. (2012). "Efficient Runge–Kutta Discontinuous Galerkin Methods Applied to Aeroacoustics". PhD thesis. KU Leuven.

Vion, A. and C. Geuzaine (2014). "Double sweep preconditioner for optimized Schwarz methods applied to the Helmholtz problem". In: *Journal of Computational Physics* 266, pp. 171–190.

Vorst, H. A. Van der (2003). *Iterative Krylov methods for large linear systems*. Vol. 13. Cambridge University Press.

Williamschen, M., G. Gabard and H. Bériot (2016). "Impact of the Mean Flow Representation on DGM Simulations of Flow Acoustics". In: *22nd AIAA/CEAS Aeroacoustics Conference*. AIAA Paper 2016-2974.